

博士論文

**Fabrication of new functional nanomaterials
by dealloying method**

(脱合金化法を用いた新規ナノ構造材料の創製と機能開発)

石川 敬章

平成 27 年

Doctoral Dissertation

**Fabrication of new functional nanomaterials
by dealloying method**

Yoshifumi Ishikawa

Supervisor: Prof. Naoki Asao

Department of Chemistry, Graduate School of Science,
Tohoku University

2015

Contents

General introduction

Chapter 1. Development of nanoporous gold catalyzed organic transformation reaction

Adapted with permission from *Angew. Chem. Int. Ed.*, **2010**, *49*, 10093-10095.

Copyright 2010 John Wiley & Sons, Inc.

Adapted with permission from *Catal. Sci. Tech.*, **2013**, *3*, 2902-2905.

Copyright 2013 Royal Society of Chemistry

Chapter 2. Fabrication of ultrafine titanate nanowires with extraordinary ion-exchange property

Adapted with permission from *Nano Lett.*, **2015**, *15*, 2980-2984.

Copyright 2015 American Chemical Society.

Chapter 3. Cerium oxide nanorods with unprecedented low temperature oxygen storage capacity

Adapted with permission from *Adv. Mater.*, **2015**, *in press*.

Copyright 2015 John Wiley & Sons, Inc.

Acknowledgement

List of Publications

Chapter 1

1. Nano-structured Materials Catalyst: Nanoporous Gold Catalyzed Oxidation of Organosilanes with Water
N. Asao, Y. Ishikawa, N. Hatakeyama, Menggenbateer, Y. Yamamoto, M. Chen, W. Zhang, A. Inoue, *Angew. Chem. Int. Ed.*, **2010**, *49*, 10093-10095.
2. Selective Hydrosilylation of Alkynes with a Nanoporous Gold Catalyst
Y. Ishikawa, Y. Yamamoto, N. Asao, *Catal. Sci. Tech.*, **2013**, *3*, 2902-2905.

Chapter 2

3. Ultrafine Sodium Titanate Nanowires with Extraordinary Sr Ion-Exchange Properties
Y. Ishikawa, S. Tsukimoto, K. S. Nakayama, N. Asao, *Nano Lett.*, **2015**, *15*, 2980-2984.

Chapter 3

4. Cerium Oxide Nanorods with Unprecedented Low-Temperature Oxygen Storage Capacity
Y. Ishikawa, M. Takeda S. Tsukimoto, K. S. Nakayama, N. Asao, *Adv. Mater*, **2015**, *in press*.

Other Publications

5. Nanostructured Zr-Pd Metallic Glass Thin Film for Biochemical Applications
S. V. Ketov, X. Shi, G. Xie, R. Kumashiro, A. Y. Churyumov, A. I. Bazlov, N. Chen, Y. Ishikawa, N. Asao, H. Wu, D. V. Louzguine-Luzgin, *Scientific Reports*, **2015**, *5*, 7799.
6. Highly efficient heterogeneous aerobic cross-dehydrogenative coupling via C–H functionalization of tertiary amines using a nanoporous gold skeleton catalyst

H. E. Ho, Y. Ishikawa, N. Asao, Y. Yamamoto, T. Jin, *Chem. Commun.*, **2015**, *51*, 12764-12767

7. The synergistic effect of nanoporous AuPd alloy catalysts on highly chemoselective 1,4-hydrosilylation of conjugated cyclic enones

Q. Chen, S. Tanaka, T. Fujita, L. Chen, T. Minato, Y. Ishikawa, M. Chen, N. Asao, Y. Yamamoto, T. Jin, *Chem. Commun.*, **2014**, *50*, 3344-3346.

8. Remarkable Catalytic Property of Nanoporous Gold on Activation of Diborons for Direct Diboration of Alkynes

Q. Chen, J. Zhao, Y. Ishikawa, N. Asao, Y. Yamamoto, T. Jin, *Org. Lett.*, **2013**, *15*, 5766-5769.

9. Nanoporous Gold Catalyst for Highly Selective Semihydrogenation of Alkynes: Remarkable Effect of Amine Additives

M. Yan, T. Jin, Y. Ishikawa, T. Minato, T. Fujita, L. -Y. Chen, M. Bao, N. Asao, M. -W. Chen, Y. Yamamoto, *J. Am. Chem. Soc.*, **2012**, *134*, 17536-17542.

10. Atomic origin of the high catalytic activity of nanoporous gold

T. Fujita, P. F. Guan, K. McKenna, X. Y. Lang, A. Hirata, L. Zhang, T. Tokunaga, S. Arai, Y. Yamamoto, N. Tanaka, Y. Ishikawa, N. Asao, Y. Yamamoto, M. W. Chen, *Nature Materials*, **2012**, *11*, 775-780.

11. Formation and properties of Au-based nanograined metallic glasses

N. Chen, R. Frank, N. Asao, D. V. Louzguine-Luzgin, P. Sharma, J. Q. Wang, G. Q. Xie, Y. Ishikawa, N. Hatakeyama, Y. C. Lin, M. Esashi, Y. Yamamoto, A. Inoue, *Acta Mater.*, **2011**, *59*, 6433-6440.

Abbreviations

Ac	acetyl group
AuNPore	nanoporous gold
aq.	aqueous
Bu	buthyl group
BET	Brunauer-Emmett-Teller
BJH	Barrett-Joyner-Halenda
Cat	catalyst
CV	cyclic voltammetry
DSSC	dye-sensitized solar cell
EDS	energy dispersive X-ray spectroscopy
EDX	energy dispersive X-ray spectroscopy
Et	ethyl group
GC	gas chromatograph
h	hour
HR	high resolution
ICP	inductively coupled plasma analysis
IR	infra-red
Me	methyl group
Min	minutes
NBDP	nano-beam diffraction pattern
NMR	nuclear magnetic resonance
OSC	oxygen storage capacity
Ph	phenyl group
Pr	propyl group
SA	surface area
SEM	scanning electron microscopy
SSA	specific surface area
STEM	scanning transmission electron microscopy
TGA	thermogravimetric analysis
TEM	transmission electron microscope
TLC	thin layer chromatography
TOF	turnover frequency
TON	turnover number

TWC	three way catalyst
UV	ultra violet
XRD	X-ray diffraction

Numbering

Compounds, Tables, Schemes, and Figure are numbered independently in each section

Introduction

General Introduction

1. Nanomaterials
2. Dealloying process
3. Gold nanomaterials
 - 3.1 Homogeneous catalyst
 - 3.2 Gold nanoparticles
 - 3.3 Nanoporous gold
4. Titanium oxide nanomaterials
 - 4.1 Titanium oxide
 - 4.2 Nanomaterials
5. Cerium oxide nanomaterials
 - 5.1 Cerium oxide
 - 5.2 Oxygen storage capacity
6. This study

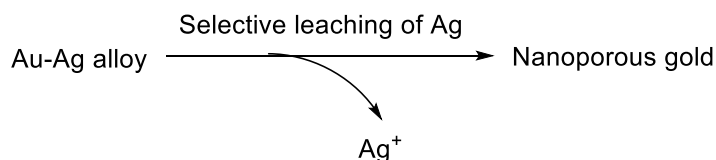
1. Nanomaterials

Nanotechnology plays a very important role in current societies.¹ By controlling of materials size in the atomic or molecular scale, many new characters can be introduced to materials.² As an example, bulky gold is chemically inactive. In contrast, gold nanoparticles which have diameter of several nanometers exhibit catalytic activities for various kinds of organic transformation reactions.³ These differences are generally explained by the high surface area and high surface energy originated by small size.⁴

The synthetic method of nanomaterials can be categorized to “Top-down” and “Bottom up” approaches. Top down approach is a fabrication method of nanomaterials by making bulky materials smaller. Lithography and milling methods are categorized to this group.⁵ On the other hand, bottom up approach is a preparation method by assembling atoms or molecules. Most of chemical approaches are categorized to the latter case.⁶

2. Dealloying process

Dealloying (selective leaching) process has received considerable attention as a synthetic method of nanomaterials.⁵ Raney nickel is a well-known catalyst for organic synthesis, which can be obtained with this method by dealloying of aluminum from a nickel – aluminum alloy with base treatment. It consists of porous structures with high specific surface area, and exhibits remarkable catalytic properties for reduction of organic molecules.⁸ In 1979, Forty has reported a fabrication method of nanoporous gold material by the selective leaching of silver from gold-silver alloy (Scheme 1).



Scheme 1. Fabrication of nanoporous gold

Nanoporous gold generally has three dimensional network structure with gold ligaments, which results in the formation of a number of pores in a range of 20 ~ 30 nanometers with high surface areas. Due to such structures, this material shows unique properties in a wide variety of applications, such as electrocatalysts,¹⁰ sensors,¹¹ actuators¹² and so on.

3. Gold nanomaterials

3.1 Homogeneous gold

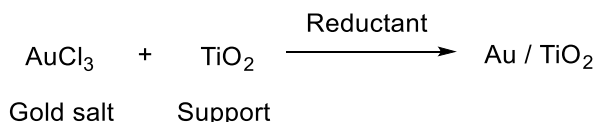
Molecular gold complexes are well known homogeneous catalysts. Such molecular golds

can catalyze various kinds of organic transformation reactions such as benzannulation reaction, hydrosilylation reaction and so on.¹³

In these type of reactions, golds act as homogeneous catalyst. Soluble gold salts HAuCl_4 and AuCl_3 are commonly used as catalyst precursors. However, the problems associated with these gold salts are highly expensive and sensitive to light and moisture. From the resource saving point of view, gold catalyst should be recovered and reused. But the reuse of homogeneous catalyst is very difficult and requires high energy.

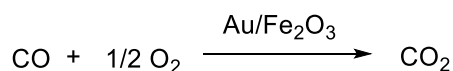
3.2 Gold nanoparticles

Gold nanoparticle is one of the most powerful heterogeneous catalyst.³ This material can be fabricated by the reduction of gold salt onto the support such as metal oxide or activated carbon (Scheme 2).



Scheme 2. Synthesis of supported gold nanoparticle

In 1987, Haruta *et. al.* reported that metallic gold particles act as powerful catalysts for CO oxidation reaction.¹⁴ In this report, they used gold nanoparticles deposited on metal oxide nanoparticles for the oxidation of carbon monoxide (Scheme 3).



Scheme 3. Oxidation of CO via gold nanoparticles

After this report, various kinds of organic transformation reactions catalyzed by gold nanoparticles were reported.

The catalytic activities of gold nanoparticles are highly dependent on the size of gold and support. In general, small particles show higher catalytic activities. One of the reason is the increasing specific surface area. When the diameter becomes small, surface area is enhanced slightly. Increase of the surface area of catalyst means the increasing catalytically active site and catalytic activity. The other reason is the quantum size effect. The electronic states of nanoparticles with the size of several nanometer are different from that of bulk state.⁴ Due to these effects, the turnover frequency of gold nanoparticles is highly dependent on the particles sizes. For many reactions, suitable size of gold is below 10 nm.^{3, 4}

In some reactions, catalysts were deactivated by the aggregation and size enhancement

of gold particles. To inhibit this aggregation, metal oxide particles or activated carbon are used as support. However, the low stability of gold nanoparticles resulted in the loss of catalytic activities due to aggregation.¹⁵

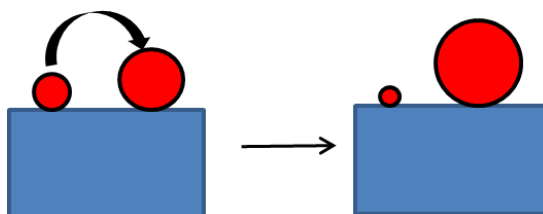


Figure 1. Ostwald ripening

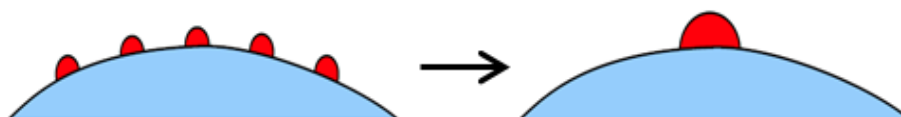


Figure 2. Migration and aggregation

The roles of the supports are improving the stability and enhancement the catalytic activity. In many cases, the catalytic activity of gold nanoparticle is highly depends on the support material. In the case of the CO oxidation, only gold nanoparticles supported on iron oxide, cobalt oxide and nickel oxide exhibited catalytic activity under $-77\text{ }^{\circ}\text{C}$.¹⁴ Enhancement of catalytic activities are explained by many reasons, such as electronic effect, molecular activation by support, acid-base effect or molecular adsorption.^{14, 16} These effects contribute to the flexibility of catalytic activities. But in some cases, they make very complicated catalytic systems. In such cases, the detail analysis and understanding of reaction systems are very difficult.

3.3 Nanoporous gold

Nanoporous gold is also well known nanomaterial. Forty *et. al* reported the first synthesis of this material.⁹ In this report, the author fabricated nanoporous gold using dealloying of silver from a gold – silver alloy (**Scheme 1**). This material have three dimensionally connected structures consisted by gold ligaments and pores (**Figure 3**).¹⁷

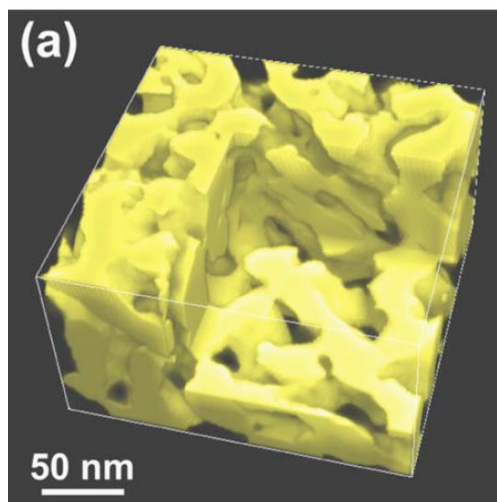
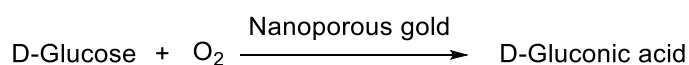


Figure 3. Three dimensional structure of nanoporous gold¹⁷

Due to its small regiment size, this material has high surface area around 10 m²/g. In addition, nanoporous gold is stable without any support due to its self-supported structure. By these unique features, many applications were reported.¹⁰⁻¹²

In spite of such unique structure and high surface area, the reports of the catalytic activity of nanoporous gold are few reported. In 2006, Bäumer *et. al.* reported the oxidation of carbon monoxide by using nanoporous gold. In this paper, author revealed the nanoporous gold shows high catalytic activity for CO oxidation. After this report, several papers of nanoporous gold catalyst were reported.¹⁹ But their reaction conditions were limited to simple gas phase or electrochemical reactions. There was only one report of nanoporous gold catalyzed liquid phase reaction, which is the simple oxidation of D-glucose (**Scheme 4**).²⁰



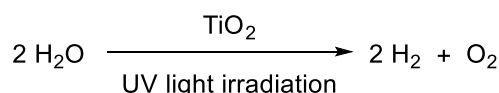
Scheme 4. Oxidation of D-Glucose catalyzed by nanoporous gold

4. Titanium oxide nanomaterials

4.1 Titanium oxide

Titanium oxide material such as titanium oxide (IV) is one of the most important metal oxide materials. Titanium oxide (IV) can adsorb UV light and generate electrons and holes. Due to this unique properties, titanium oxides are used as photo catalyst, antibacterial agents, dye sensitized solar cells and so on.²¹ Water splitting reaction (**Scheme 5**) is the most challenging reaction because this technology can generate fuel from sunlight and water without generation of carbon dioxide. The most important

finding of this research was Honda-Fujishima effect reported in 1972.²² In this reaction, hydrogen gas was generated by the reduction of protons and oxygen was generated by the oxidation of oxide anions. From this first report, various kinds of photocatalysts were reported. But these efficiencies were still not high enough and required more powerful catalytic systems.²³



Scheme 5. Water splitting reaction

The other important titanium oxides are titanate salts and hydrogen titanates.²⁴ These materials were used not only as TiO₂ precursors but also photocatalysts. Strontium titanate and potassium titanate are well known photo catalysts. Total splitting reaction of water was achieved by the combination of strontium titanate and tungsten oxide in 2011.^{25,26} Titanates can keep cations in interlayer. These ions can be exchanged to the other ions such as Ca²⁺ and Sr²⁺. Using this property, titanate materials have gathered considerable attention as radioactive ion trappers.²⁷

4.2 Nanomaterials

Many kinds of titanium oxide nanostructures are synthesized in various ways.²⁸ One dimensional titanate nanomaterials such as nanowires and nanotubes were commonly synthesized by the hydrothermal method, sol-gel method and template method.²⁹

Titanium oxide nano-sheets have two dimensional structures and synthesized commonly by exfoliation of titanium oxide.³⁰ Structure of these materials are quite unique and many applications were reported such as electrocatalysts and biomaterials.³¹

Three dimensional titanate nanomaterials have also been reported. These materials were synthesized commonly by template methods and anodizations³². In the case of template methods, surfactants or other porous materials are used to control structures. Molecular structure and concentration affect to the nanostructure and sizes. Anodization means electrical etching of titanium metals or titanium contained alloys.

Oxidation of titanium is occurred by the electrolysis and some parts are leached while some parts are remained as titanium oxide nanostructures. These three dimensional titanium oxide nanomaterials were used as powerful electrocatalysts, DSSCs and so on.

5. Cerium oxide nanomaterials

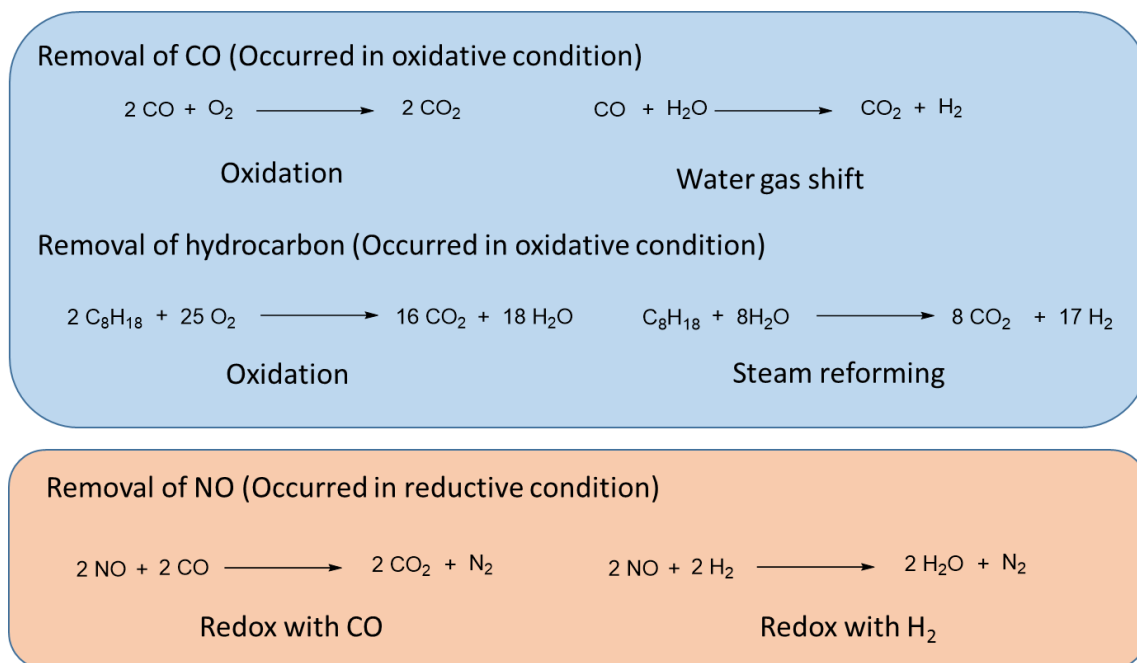
5.1 Cerium oxide

Metallic cerium is easily oxidized in air and Cerium (IV) oxide is formed. Cerium (IV) oxides is very stable metal oxide having pale yellow color. This material is commonly used as polisher of glasses. In this use, cerium oxide polishes glass not only mechanically but also chemically.³³ In addition, cerium oxides are used as photo catalysts³⁴ and UV blockers³⁵ due to their UV adsorption abilities.

5.2 Oxygen storage capacity

One of the most important applications of cerium oxide is the support of three way catalysts (TWCs) by their oxygen storage capacities (OSC). In TWCs, hydrocarbons, carbon monoxide and nitrogen oxides are converted to carbon dioxide, water, and nitrogen gas.³⁶

In order to achieve high conversion of harmful components, the air: fuel ratio is important because hydrocarbons and carbon monoxide are converted under oxidative condition and, the nitrogen oxides are converted under reductive condition (**Scheme 6**). To achieve high conversion, the air: fuel ratio is needed to be kept 14.7 called “stoichiometric region” (**Figure 4**).



Scheme 6. Reactions in TWCs

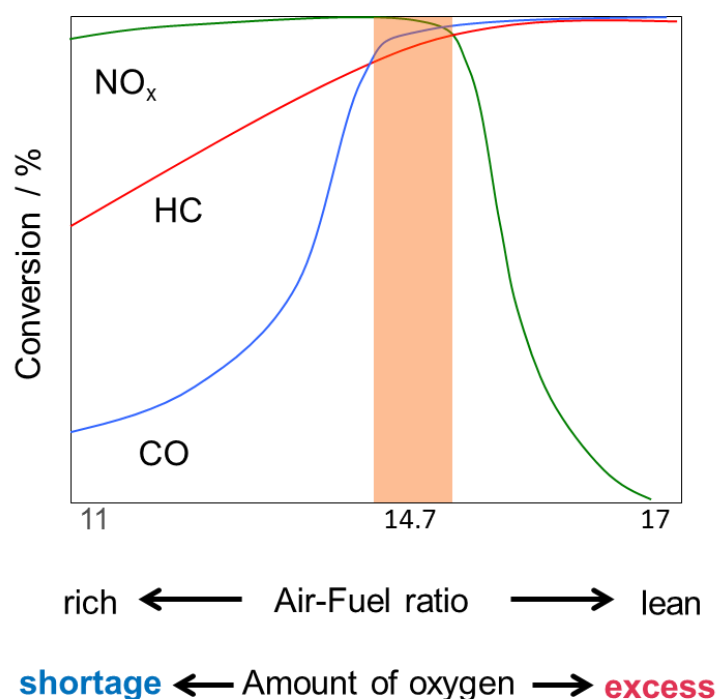
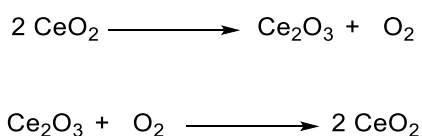


Figure 4. Image of stoichiometric region

Cerium oxide supports TWCs with its oxygen storage ability. When air: fuel ratio becomes less than 14.7, exhaust gas becomes reductive condition. In this case, hydrocarbons and carbon monoxide can't be oxidized. In such condition, cerium oxide releases oxygen and oxidize hydrocarbons and carbon monoxide. On the other hand, when air: fuel ratio become over than 14.7, Ce₂O₃ reacts with oxygen and keep high conversion of nitrogen oxides (**Scheme. 7**).³⁶

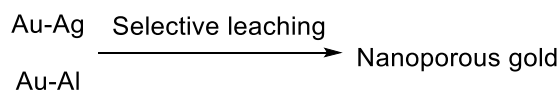


Scheme 7. Reaction of ceria as OSC materials

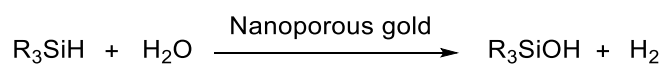
Recently, the development of low temperature TWCs is strongly required for future fuel efficient vehicles for the protection of the environment.³⁷ In this regard, considerable efforts have been made to design and synthesize a variety of cerium oxide nanomaterials.³⁸

5. This study

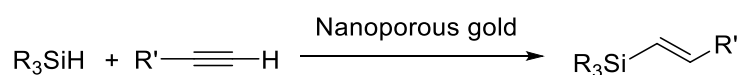
The purpose of this study is to discover new functional nanomaterials by a dealloying method. In chapter 1, I have succeeded in development of new catalytic functionalities of nanoporous gold materials in heterogeneous organic molecular transformation reactions.



Scheme 8. Fabrication of nanoporous gold

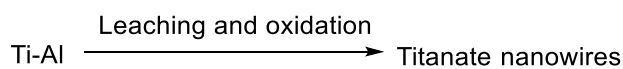


Scheme 9. Oxidation of organosilanes (chapter 1)

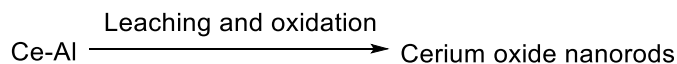


Scheme 10. Hydrosilylation reaction (chapter 1)

In chapters 2 and 3, I combined the dealloying method with the oxidation process and created new functional nanomaterials. Titanate nanowires fabricated from a Ti-Al alloy exhibited an excellent strontium ion exchange ability (Chapter 2). Cerium oxide nanorods obtained from a Ce-Al alloy exhibited a high oxygen storage capacity under low temperatures.



Scheme 11. Fabrication of titanate nanowires (chapter 2)



Scheme 12. Fabrication of cerium oxide nanorods (chapter 3)

Reference

1. a) H. Dai, *Acc. Chem. Res.*, **2002**, *35*, 1035
b) A. T. Bell, *Science* **2003**, *299*, 1688
c) S. M. Moghimi, A. C. Hunter, J. C. Murray, *FASEB J.* **2005**, *19*, 311
2. a) C. Burda, X. B. Chen, R. Narayanan, M. A. E- Sayed, *Chem. Rev.*, **2005**, *105*, 1025
b) P. V. Kamat, *J. Phys. Chem. C*, **2007**, *111*, 2834
c) P. G. Bruce, B. Scrosati, J. M. Tarascon, *Angew. Chem. Int. Ed.*, **2008**, *47*, 2930
d) X. Y. Huang, S. Y. Han, W. Huang, X. G. Liu, *Chem. Soc. Rev.*, **2013**, *42*, 173
3. a) C. Della Pina, E. Falletta, L. Prati, M. Rossi, *Chem. Soc. Rev.* **2008**, *37*, 2077
b) A. Corma, H. Garcia, *Chem. Soc. Rev.* **2008**, *37*, 2096
c) R. Sardar, A. M. Funston, P. mulvaney, R. W. Murray, *Langmuir*, **2009**, *25*, 13840
d) V. Polshettiwar, R. S. Varma, *Green Chem.*, **2010**, *12*, 743
e) M. Stratakis, H. Garciam *Chem. Rev.* **2012**, *112*, 4469
f) G. Li, R. C. Jin, *Acc. Chem. Res.*, **2013**, *46*, 1749
4. M. Haruta, M. Date, *Appl. Catal. A* **2001**, *222*, 427
5. H. D. Yu, M. D. Refulacio, E. Ye, M. Y. Han, *Chem. Soc. Rev.*, **2013**, *42*, 6006
6. a) X. Wang, J. Zhuang, Q. Peng, Y. D. Li *Nature* **2005**, *437*, 121
b) K. Ariga, J. P. Hill, M. V. Lee, A. Vinu, R. Charvet, S. Acharya *Sci. Tech. Adv. Mater.*, **2008**, *9*, 014109
c) K. Ariga, Y. Yamauchim G. Rydzek, Q. M. Ji, Y. Yonamine, K. C. W. Wu, J. P. Hill, *Chem. Lett.*, **2014**, *43*, 36
7. B. Harry, A. Homer, *Org. Synth.* **1949**, *29*, 49
8. R. Mozingo, D. E. Wolf, S. A. Harris, K. Folkers, *J. Am. Chem. Soc.*, **1943**, *65*, 1013
9. A. J. Forty, *Nature* **1979**, *282*, 597
10. L. C. Nagle, J. F. Rohan, *Int. J. Hydrogen Energy* **2011**, *36*, 10319
11. J. Biener, G.W. Nyce, A. M. Hodge, M. M. Biener, A. V. Hamza, S. A. Maier, *Adv. Mater.* **2008**, *20*, 1211
12. J. Biener, A. Wittstock, L. A. Zepeda-Ruiz, M. M. Biener, V. Zielasek, D. Dramer, R. N. Viswanath, J. Weissmuller, M. Baumer, A. V. Hamza, *Nat. Mater.* **2009**, *8*, 47

13. a) N. Asao, T. Sudo, Y. Yamamoto, *J. Org. Chem.*, **1996**, *61*, 7654
 b) T. Sudo, N. Asao, V. Gevorgyan, Y. Yamamoto, *J. Org. Chem.*, **1999**, *64*, 2494
 c) A. S. K. Hashimi, G. J. Hutchings, *Angew. Chem. Int. Ed.*, **2006**, *45*, 7896
 d) A. S. K. Hashimi, M. Rudolph, *Chem. Soc. Rev.*, **2008**, *37*, 1766
 e) D. J. Gorin, B. D. Sherry, F. D. Toste, *Chem. Rev.*, **2008**, *108*, 3351

14. M. Haruta, T. Kobayashi, H. Sano, N. Yamada, *Chem. Lett.* **1987**, *16*, 405

15. a) D. X. Li, Q. He, Y. Chi, L. Duan, J. B. Li, *Biochem. Biophys. Res. Commun.*, **2008**, *355*, 488
 b) S. Panigrahi, S. Basu, S. Praharaj, S. Pande, S. Jana, S. A. Pal, S. K. Ghosh, T. Pal, *J. Phys. Chem. C*, **2007**, *111*, 4596
 c) Z. F. Ma, T. Ding, *Nanoscale Res. Lett.*, **2009**, *4*, 1236

16. a) A. Verma, F. Stellacci, *Small* **2010**, *6*, 12
 b) A. Corma, A. Leyva-Pérez, M. J. Sabater, *Chem. Rev.*, **2011**, *111*, 1657
 c) Y. Zhang, X. Cui, F. Shi, Y. Deng, *Chem. Rev.*, **2012**, *112*, 2467
 d) M. Stratakis, H. Garcia, *Chem. Rev.*, **2012**, *112*, 4469.

17. T. Fujita, L. H. Qian, K. Inoke, J. Erlebacher, M. W. Chen, *Appl. Phys. Lett.*, **2008**, *92*, 251902

18. V. Zielasek, B. Jürgen, C. Schulz, J. Biener, M. M. Biener, A. V. Hamza, M. Bäumer, *Angew. Chem. Int. Ed.*, **2006**, *45*, 8241

19. a) C. Xu, J. Su, X. Xu, P. Liu, H. Zhao, F. Tian, Y. Ding, *J. Am. Chem. Soc.* **2007**, *129*, 42
 b) C. Xu, X. Xu, J. Su, Y. Ding, *J. Catal.* **2007**, *252*, 243
 c) A. Wittstock, B. Neumann, A. Schaefer, K. Dumbuya, C. Kubel, M. M. Biener, V. Zielasek, H.-P. Steinrück, J. M. Gottfried, J. Biener, A. Hamza, M. Baumer, *J. Phys. Chem. C* **2009**, *113*, 5593
 d) H. Yin, C. Zhou, C. Xu, P. Liu, X. Xu, Y. Ding, *J. Phys. Chem. C* **2008**, *112*, 9673
 e) A. Wittstock, V. Zielasek, J. Biener, C. M. Friend, M. Baumer, *Science* **2010**, *327*, 319
 f) J. Zhang, P. Liu, H. Ma, Y. Ding, *J. Phys. Chem. C* **2007**, *111*, 10382
 g) C. Yu, F. Jia, Z. Ai, L. Zhang, *Chem. Mater.* **2007**, *19*, 6065
 h) R. Zeis, T. Lei, K. Sieradzki, J. Snyder, J. Erlebacher, *J. Catal.* **2008**, *253*, 132

20. H. M. Yin, C. Q. Zhou, C. X. Xu, P. P. Liu, X. H. Xu, Y. Ding, *J. Phys. Chem. C*, **2008**, *112*, 9673

21. a) M. R. Hoffmann, S. T. Martin, W. Y. Choi, D. W. Bahnemann, *Chem. Rev.*, **1995**, *95*, 69
 b) A. Fujishima, X. T. Zhang, D. A. Dryk, **2008**, *63*, 515
 c) A. Kubacka, M. Fernandex-Garcia, G. Colon, **2012**, *112*, 1555
22. A. Fujishima, K. Honda, *Nature*, **1972**, *238*, 37
23. a) A. Kudo, Y. Miseki, *Chem. Soc. Rev.*, **2009**, *38*, 253
 b) T. Hisatomi, J. Kubota, K. Domen, *Chem. Soc. Rev.*, **2014**, *43*, 7520
24. a) N. Z. Bao, X. Feng, Z. H. Yang, L. M. Shen, X. H. Lu, *Environ. Sci. Technol.* **2004**, *38*, 2729
 b) K. Maeda, *ACS Catal.* **2013**, *3*, 1486
25. K. Sayama, K. Mukasa, R. Abe, Y. Abe, H. Arakawa, *Chem. commun.* **2001**, *23*, 2416
26. K. Vaaramaa, J. Lehto *Desalination*, **2003**, *155*, 157
27. a) D. J. Yang, Z. F. Zheng, H. Y. Zhu, H. W. Liu, X. P. Gao, *Adv. Mater.* **2008**, *20*, 2777.
 b) D. J. Yang, Z. F. Zheng, H. W. Liu, H. Y. Zhu, X. B. Ke, Y. Xu, D. Wu, Y. Sun, *J. Phys. Chem. C*, **2008**, *112*, 16275
28. X. Chen, S. S. Mao, *Chem. Rev.*, **2007**, *107*, 2891
29. a) Z. Y. Yuan, B. L. Su, *Colloid. Surf.* **2004**, *241*, 173
 b) S. V. N. T. Kuchibhatla, A. S. Karakoti, D. Bera, S. Seal, *Prog. Mater. Sci.* **2007**, *52*, 699
30. a) T. Tanaka, Y. Ebina, K. Takada, K. Kurashima, T. Sasaki, *Chem. Mater.*, **2003**, *15*, 3564
 b) Y. Ide, M. Sadakane, T. Sano, M. Ogawa, *J. Nanosci. Nanotechnol.*, **2014**, *14*, 2135
31. a) M. Osuda, T. Sasaki, *Adv. Mater.*, **2012**, *24*, 210
 b) M. Li, Y. Ishida, Y. Ebina, T. Sasaki, T. Hikima, M. Tanaka, T. Aida, *Nature*, **2015**, *517*, 68
32. a) V. Zwillig, M. Aucouturier, E. D. Ceretti, *Electrochem. Acta*, **1999**, *45*, 921
 b) R. Beranek, H. Hildebrand, P. Schmki, *Electrochem. Solid State Lett.* **2003**, *6*, B12
 c) D. G. Shuhukin, R. A. Caruso, *Chem. Mater.*, **2004**, *16*, 2287
 d) D. Gong, C. A. Grimes, O. K. Varghese, *J. Mater. Res.*, **2011**, *16*, 3331
33. Y. Sampurno, F. Sudargho, Y. Zhuang, T. Ashizawa, H. Morishima, A. Philipossian,

- Electrochem. Solid State Lett.* **2009**, *12*, H191
34. a) Y. Zhai, S. Zhang, H. Pang, *Mater. Lett.*, **2007**, *61*, 1863
 b) P. F. Ji, J. L. Zhang, F. Chen, M. Anpom *Appl. Catal. B*, **2008**, *85*, 148
 c) H. R. Pouretedal, A. Kadjodaie *Chinese J. Catal.*, **2010**, *31*, 1328
35. K. Anupriya, E. Vivek, B. Subramanian, *J. Alloy. Comp.* **2014**, *590*, 406
36. J. Kaspar, P. Fornasiero, M. Graziani, *Catal. Today*, **1999**, *50*, 285
37. H.-Y. Chen, H.-L. Chang, *J. M. Technol. Rev.* **2015**, *59*, 64.
38. a) Q. Yuan, H.-H. Duan, L.-L. Li, L.-D. Sun, Y.-W. Zhang, C.-H. Yan, *J. Colloid Interface Sci.* **2009**, *335*, 151.
 b) A. Bumajdad, J. Eastoe, A. Mathew, *Adv. Colloid Interface Sci.* **2009**, *56*, 147.
 c) C. W. Sun, H. Li, L. Q. Chen, *Energy Environ. Sci.* **2012**, *5*, 8475.
 d) D. Zhang, X. Du, L. Shi, R. Gao, *Dalton Trans.* **2012**, *41*, 14455.
 e) N. Ta, J. Liu, W. Shen, *Chin. J. Catal.* **2013**, *34*, 838.
 f) Z. A. Qiao, Z. Wu, S. Dai, *ChemSusChem* **2013**, *6*, 1821.
 g) W. Huang, Y. Gao, *Catal. Sci. Technol.* **2014**, *4*, 3772.

Chapter 1

Development of nanoporous gold catalyzed
organic transformation reaction.

Section 1

Nanoporous gold catalyzed oxidation of organosilanes with water

1, Introduction

Molecular transformations with a single atom / single molecular gold catalysts are becoming a processing concern to organic and catalytic chemists.¹ On the other hand, bulk gold metal does not exhibit catalytic activity. It is known that small gold particles in the range of 2 to 5 nm on suitable support show catalytic activities in a wide variety of molecular transformations in gas and liquid phases.²

More recently, nanoporous gold (AuNPore) nanostructured materials has attracted much attention as sensors³ and actuators⁴ and so on. Recently, some reactions catalyzed by nanoporous gold were reported.⁵⁻⁷ But these reactions mainly focused on simple gas phase or electrochemical reaction and simple liquid phase reaction was quite few.

Silanols are useful building blocks for silicon-based polymeric materials⁸ as well as nucleophilic coupling partners in organic synthesis.⁹ Although a variety of preparation methods of Silanols have been developed, oxidations of organosilanes with water catalyzed by heterogeneous catalysts, such as supported metal nanoparticle catalysts, would be ideal from an environmental viewpoint because the catalyst is reusable and the co-product is only hydrogen gas. For example, Kaneda and co-workers reported that hydroxyapatite-supported gold nanoparticles were effective catalysts for this transformation.^{10, 11} However, there are some drawbacks in those cases, such as decrease of catalytic activity owing to agglomeration, limited scope to certain substrate types, formation of disiloxanes derived from the condensation of silanols, and cumbersome work-up procedures for separation of products from the catalyst.

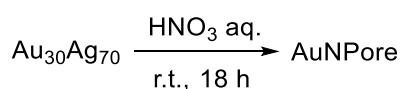
Here, we show how nanoporous gold exhibits a remarkable catalytic activity in the oxidation of a wide range of organosilanes. The corresponding silanols can be produced in high yields under mild conditions together with the evolution of hydrogen gas. Furthermore, the catalyst can be reused several times and the work-up process is quite simple.

After our report, some of powerful catalytic systems were newly reported. For example,

gold nanoparticles anchored to carbon nanotubes exhibited excellent catalytic activity for this reaction. Even compared with these new reaction systems, simplicity of the nanoporous gold system is outstanding and importance is high because no need to used filtering or centrifugation to catalyst recycles.

2, Result and discussion

The nanoporous gold catalyst used in this study was prepared by the selective leaching of silver from gold-silver solid solution foil. As the mother alloy composition, I choose the $\text{Au}_{30}\text{Ag}_{70}$ alloy (in atom %).¹² In the case of $\text{Au}_{35}\text{Ag}_{65}$ alloy, it required over 2 days for dealloying. On the other hand, nanoporous gold fabricated from the mother alloy of $\text{Au}_{20}\text{Ag}_{80}$ alloy can't keep foil macrostructure and not suitable for reusing. From these result, we choose the $\text{Au}_{30}\text{Ag}_{70}$ alloy foil of 40 μm thickness as mother alloy. By the treatment of 70 wt% HNO_3 for 18 h, nanoporous gold catalyst was fabricated.



Scheme 1.1 Synthesis of nanoporous gold

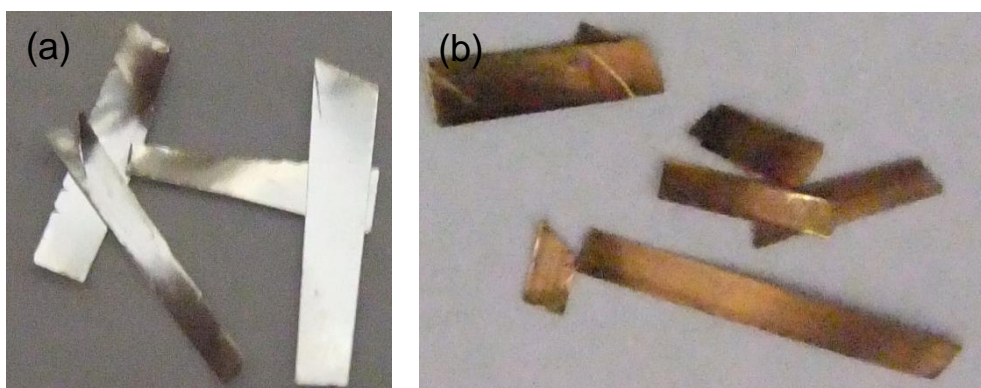


Figure 1.1 Picture of $\text{Au}_{30}\text{Ag}_{70}$ alloy foil (a) and AuNPore (b)

Figure 1.2 shows the SEM image of obtained nanoporous gold. As shown in here, the nano pore size was measured around 30 nm.

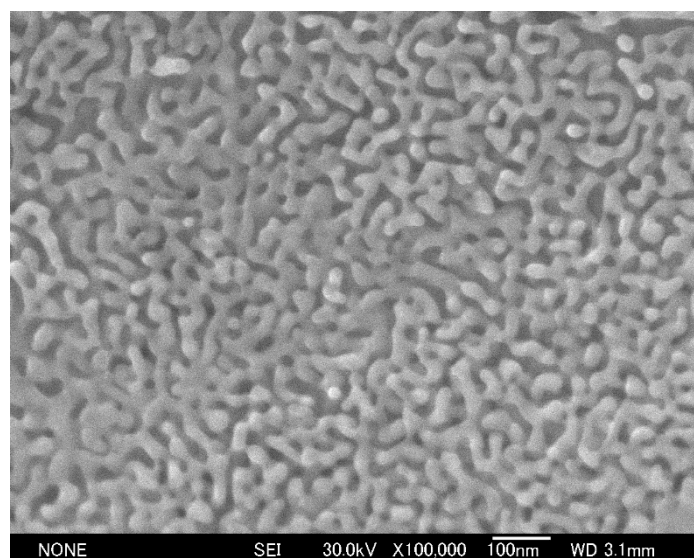
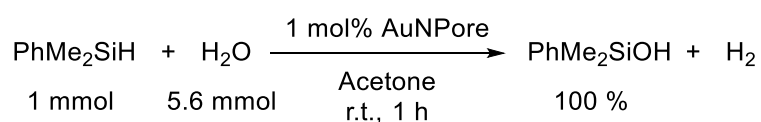


Figure 1.2 SEM image of AuNPore

Surface area was measured to around 10 m²/g by electrochemical analysis.

The reaction of PhMe₂SiH with water in the presence of the AuNPore catalyst was carried out (Scheme 1.2). When PhMe₂SiH was treated with 1 mol% of AuNPore catalyst at room temperature in aqueous acetone, hydrogen gas was evolved immediately (Figure 1.3). The gas production ceased within one hour and dimethylphenylsilanol was obtained quantitatively.



Scheme 1.2 Oxidation of organosilanes with water



Figure 1.3 Picture of reaction. Hydrogen gas is generated in from the nanoporous gold.

Initial reaction speed is needed for the turnover frequency calculation. I plotted the amount of generated hydrogen gas (Figure 1.4 and 1.5) and calculated the reaction speed was 3.01 s^{-1} (Scheme 1.3).

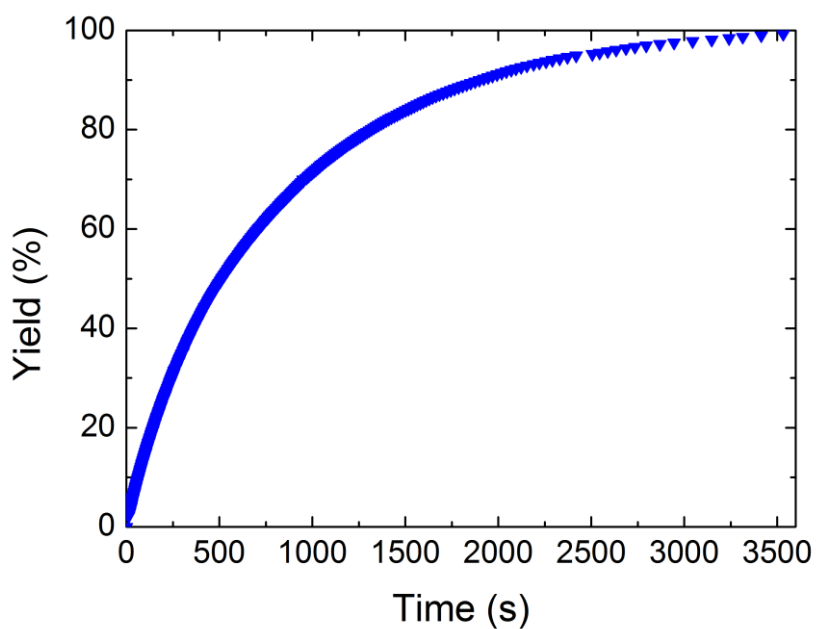


Figure 1.4 Plot of generated hydrogen amount

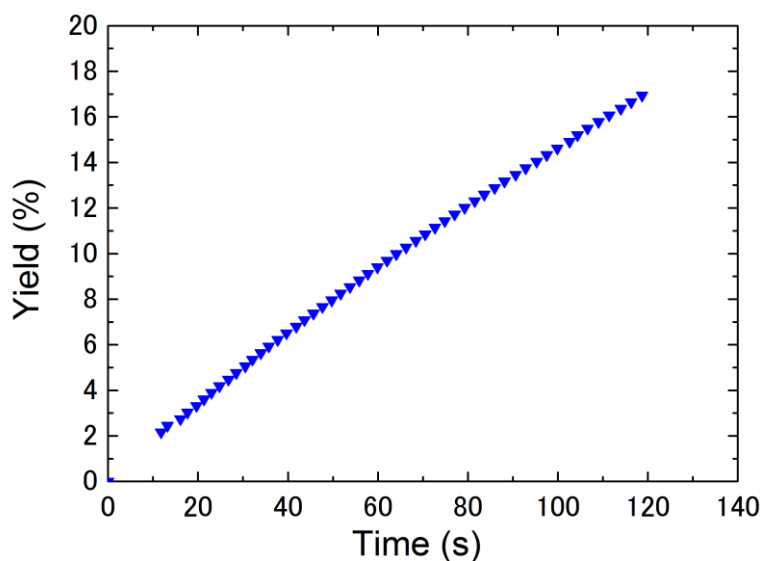


Figure 1.5 Expanded image of Figure 1.4.

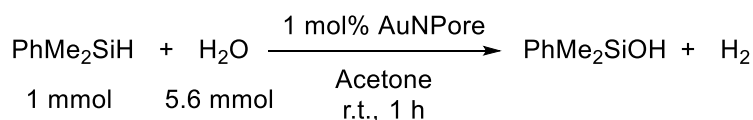
$$\begin{aligned}
 \text{Turnover frequency} &= \frac{\text{Amount of Product}}{\text{Amount of surface gold atom} \times \text{Time}} \\
 &= \frac{0.14 \times 1/100 \times 1/1000 \times 6.02 \times 10^{23}}{2.0 \times 1/1000 \times 10 \times 1.4 \times 10^{19} \times 1} \\
 &= 3.01 \text{ [s}^{-1}\text{]}
 \end{aligned}$$

Scheme 1.3 Calculation of turnover frequency

On the other hand, only the trace amount of silanols was obtained in the oxidation reaction of silanes with simple gold foil having no porous structure. These results clearly indicated that the nanostructure of the catalyst plays a crucial role for the current transformations. It is noteworthy that the formation of disiloxane, 1,1,3,3-tetramethyl-1,3-diphenyldisiloxane, was not detected at all by GC-MS.

Generally, the recovery of the heterogeneous catalyst was carried out by filtration or centrifugation for the separation of the catalyst from the reaction system. In the presence system, I used some small pieces of the nanostructured gold foil as a catalyst with the size of around 5×2 mm (Figure 1.1). Thus, the catalyst can be reused easily by picking

up by tweezers without any cumbersome work-up processes. After a simple washing of the catalyst with dimethyl ether, it was reused without further purification. I used the catalyst repeatedly (five times), but no significant loss of activity was observed (Table 1.1). The product was obtained nearly quantitatively every time and the turnover (TON) reached up to 10700 (Scheme 1.4). Figure 1.6 is the SEM image of the recovered catalyst after 5 time uses. No significant changes were observed in comparison with Figure 1.2.



Entry	Catalyst	Yield of silanol [%]
1	fresh	100
2	reuse 1	98
3	reuse 2	100
4	reuse 3	99
5	reuse 4	100

Table 1.1 Reusing test

$$\begin{aligned} \text{Turnover number} &= \frac{\text{Amount of Product}}{\text{Amount of surface gold atom}} \\ &= \frac{(1+0.98+1+0.99+1) \times 1/1000 \times 6.02 \times 10^{23}}{2.0 \times 1/1000 \times 10 \times 1.4 \times 10^{19}} \\ &= 10700 \end{aligned}$$

Scheme 1.4 Calculation of turnover number

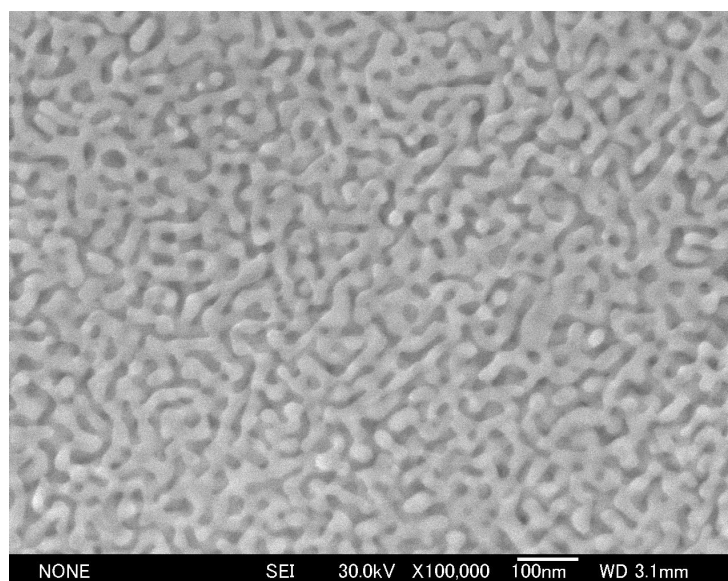
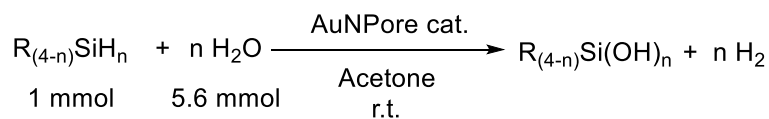


Figure 1.6 SEM image of AuNPore after being used five times

The catalytic oxidation reactions with variety of organosilanes were then carried out (Table 1.2). Not only aromatic silanes but also trialkylsilanes were oxidized effectively (entry 1-3). The reaction of sterically less-hindered triethylsilane proceeded smoothly in 2 h and the desired triethylsilanol was produced in 94% yield (entry 1). Even with sterically hindered trialkylsilanes, such as tributylsilane and triisopropylsilane, the corresponding silanols were obtained in high yield by increasing the catalyst loading to 3 mol% (entries 2 and 3). On the other hand, the reaction of sterically hindered triphenylsilane proceeded with 1 mol% of the catalyst, and the corresponding silanol was obtained nearly quantitatively (entry 4). The AuNPore catalyst could also be used in the oxidation of diphenylsilanes and phenylsilane and the corresponding oxygenated products, diphenylsilanediol and phenylsilanetriol, were obtained in 90 and 80% yield respectively (entries 5 and 6). Alkenyl- and alkynyl containing silanols were suitable substrates for the current oxidation reaction, and the corresponding silanols were obtained in high yields without hydrogenation reaction (entries 7 and 8).



Entry	R _(4-n) SiH _n	Cat. [mol%]	t [h]	Yield of silanol [%]
1	Et ₃ SiH	1	2	94
2	Bu ₃ SiH	3	3	95
3	iPr ₃ SiH	3	5	88
4	Ph ₃ SiH	1	5	99
5	Ph ₂ SiH ₂	1	9	90
6	PhSiH ₃	5	6	80
7	(H ₂ C=CH)MePhSiH	1	1	98
8	(PhCC)Me ₂ SiH	3	1.5	92

Table 1.2 Scope of the oxidation of organosilanes

We then examined the reaction to clarify whether the dissolved gold species in solvents take part in the current molecular transformation or not. After the catalytic oxidation of dimethylphenylsilane was carried out for 10 min under the standard conditions, the nanoporous gold was removed from the reaction vessel. ¹HNMR analysis of the mixture showed that product was produced in 48% yield at this time. While stirring of the mixture was continued in the absence of the catalyst for 50 min, further consumption of silane was not detected at all. AuNPore was then put back into the mixture. The oxidation reaction restarted immediately and finally silanols was obtained in 99% yield within 50 min (Figure 1.7). It is also worth mentioning that leaching of the gold in the reaction of silanes was not detected by ICP analysis (<0.0005%). These results clearly indicated that the current transformation was catalyzed by the AuNPore catalyst surface.

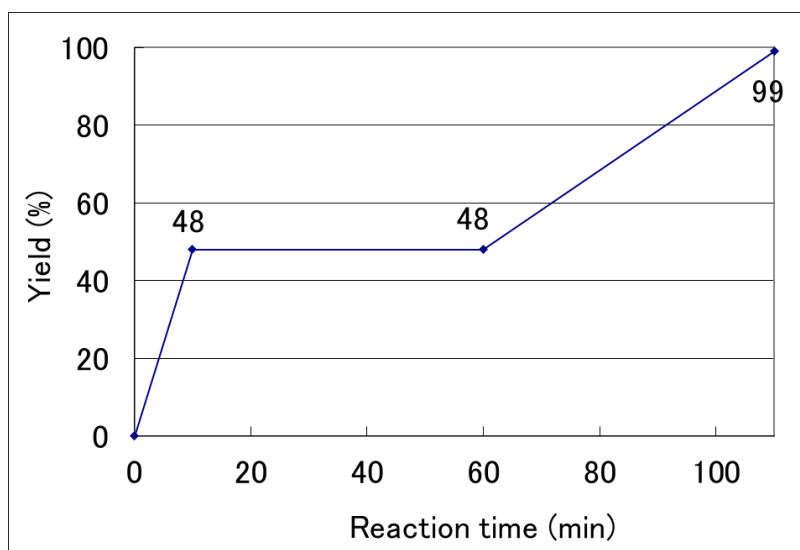


Figure 1.7 Leaching test

In conclusion, I have discovered that a nanoporous gold materials exhibited a remarkable catalytic activity in the oxidation of organosilanes compounds with water. The catalyst was easily recoverable and could be reused at least five times without leaching and loss of activity. The observed excellent durability of the catalyst was also confirmed by SEM images. Indeed, the nanoporous structure of the catalyst did not change, even after five time uses for the oxidation of organosilanes. Further studies to elucidate the mechanism of this reaction and extend the scope of synthetic utility are in progress.

3. Reference

1. a) E. Jimenez-Nunez, A. M. Echavarren, *Chem. Commun.* **2007**, 333
b) D. J. Gorin, F. D. Toste, *Nature* **2007**, *446*, 395
c) A. S. K. Hashmi, *Chem. Rev.* **2007**, *107*, 3180
d) A. Furstner, P.W. Davies, *Angew. Chem. Int. Ed.* **2007**, *46*, 3410
e) N. T. Patil, Y. Yamamoto, *Chem. Rev.* **2008**, *108*, 3395
f) H. C. Shen, *Tetrahedron* **2008**, *64*, 3885
g) R. Skouta, C.-J. Li, *Tetrahedron* **2008**, *64*, 4917
h) Z. Li, C. Brouwer, C. He, *Chem. Rev.* **2008**, *108*, 3239
i) Y. Yamamoto, I. D. Gridnev, N. T. Patil, T. Jin, *Chem. Commun.* **2009**, 5075
j) A. Furstner, *Chem. Soc. Rev.* **2009**, *38*, 3208
k) A. S. K. Hashmi, *Angew. Chem. Int. Ed.* **2010**, *49*, 5232
2. a) C. Della Pina, E. Falletta, L. Prati, M. Rossi, *Chem. Soc. Rev.* **2008**, *37*, 2077
b) A. Corma, H. Garcia, *Chem. Soc. Rev.* **2008**, *37*, 2096
3. a) J. Biener, G.W. Nyce, A. M. Hodge, M. M. Biener, A. V. Hamza, S. A. Maier, *Adv. Mater.* **2008**, *20*, 1211
b) K. Bonroy, J.-M. Friedt, F. Frederix, W. Laureyn, S. Langerock, A. Campitelli, M. Sara, G. Borghs, B. Goddeeris, P. Declerck, *Anal. Chem.* **2004**, *76*, 4299
c) M. Hieda, R. Garcia, M. Dixon, T. Daniel, D. Allara, M. H.W. Chan, *Appl. Phys. Lett.* **2004**, *84*, 628
4. a) D. Kramer, R. N. Viswanath, J. Weissmueller, *Nano Lett.* **2004**, *4*, 793
b) J. Biener, A. Wittstock, L. A. Zepeda-Ruiz, M. M. Biener, V. Zielasek, D. Dramer, R. N. Viswanath, J. Weissmuller, M. Baumer, A. V. Hamza, *Nat. Mater.* **2009**, *8*, 47
5. a) V. Zielasek, B. Jurgens, C. Schulz, J. Biener, M. M. Biener, A. V. Hamza, M. Baumer, *Angew. Chem. Int. Ed.* **2006**, *45*, 8241
b) C. Xu, J. Su, X. Xu, P. Liu, H. Zhao, F. Tian, Y. Ding, *J. Am. Chem. Soc.* **2007**, *129*, 42
c) C. Xu, X. Xu, J. Su, Y. Ding, *J. Catal.* **2007**, *252*, 243
d) A. Wittstock, B. Neumann, A. Schaefer, K. Dumbuya, C. Kubel, M. M. Biener, V. Zielasek, H.-P. Steinruck, J. M. Gottfried, J. Biener, A. Hamza, M. Baumer, *J. Phys. Chem. C* **2009**, *113*, 5593

6. a) H. Yin, C. Zhou, C. Xu, P. Liu, X. Xu, Y. Ding, *J. Phys. Chem. C* **2008**, *112*, 9673
 b) A. Wittstock, V. Zielasek, J. Biener, C. M. Friend, M. Baumer, *Science* **2010**, *327*, 319

7. a) J. Zhang, P. Liu, H. Ma, Y. Ding, *J. Phys. Chem. C* **2007**, *111*, 10382
 b) C. Yu, F. Jia, Z. Ai, L. Zhang, *Chem. Mater.* **2007**, *19*, 6065
 c) R. Zeis, T. Lei, K. Sieradzki, J. Snyder, J. Erlebacher, *J. Catal.* **2008**, *253*, 132

8. a) E.W. Colvin, *Silicon Reagents in Organic Synthesis*, Academic Press, London, **1988**
 b) V. Chandrasekhar, R. Boomishankar, S. Nagendran, *Chem. Rev.* **2004**, *104*, 5847
 c) R. Murugavel, M. G. Walawalkar, M. Dan, M.W. Roesky, C. N. R. Rao, *Acc. Chem. Res.* **2004**, *37*, 763

9. a) S. E. Denmark, R. F. Sweis in *Metal-Catalyzed Cross-Coupling Reactions*, Vol. 1 (Eds.: de A. Meijere, F. Diederich), Wiley-VCH, Weinheim, **2004**, chap. 4
 b) K. Hirabayashi, Y. Nishihara, A. Mori, T. Hiyama, *Tetrahedron Lett.* **1998**, *39*, 7893
 c) K. Hirabayashi, J. Kawashima, Y. Nishihara, A. Mori, T. Hiyama, *Org. Lett.* **1999**, *1*, 299
 d) S. E. Denmark, D. Wehrli, *Org. Lett.* **2000**, *2*, 565

10. T. Mitsudome, A. Noujima, T. Mizugaki, K. Jitsukawa, K. Kaneda, *Chem. Commun.* **2009**, 5302

11. a) K. Mori, M. Tano, T. Mizugaki, K. Ebitani, K. Kaneda, *New J. Chem.* **2002**, *26*, 1536
 b) E. Choi, C. Lee, Y. Na, S. Chang, *Org. Lett.* **2002**, *4*, 2369
 c) T. Mitsudome, S. Arita, H. Mori, T. Mizugaki, K. Jitsukawa, K. Kaneda, *Angew. Chem. Int. Ed.* **2008**, *47*, 7938
 d) B. P. S. Chauhan, A. Sarkar, M. Chauhan, A. Roka, *Appl. Organomet. Chem.* **2009**, *23*, 385

12. a) A. J. Forty, *Nature* **1979**, *282*, 597
 b) J. Erlebacher, M. Aziz, A. Karma, *Nature* **2001**, *410*, 450

4. Experimental section

General information

ICP analysis was performed on Shimadzu ICPS-7510 equipment. GC-MS analysis was performed on an Agilent 6890N GC interfaced to an Agilent 5973 mass-selective detector (30 m x 0.25 mm capillary column, HP-5MS). MS analysis was conducted on Hitachi M-2500 at 70 eV ionization energy. Scanning electron microscope (SEM) observation was carried out using a JEOL JSM-6500F instrument operated at an accelerating voltage of 30 kV.

Fabrication of Nanoporous Gold Catalyst

Au (99.99%) and Ag (99.99%) were melted with electric arc-melting furnace under Ar atmosphere to form Au/Ag alloy (30:70, in at. %), which was rolled down to thickness of 0.04 mm. The foil was cut into small pieces (5 x 2 mm square). Treatment of the resulting chips (67.1 mg) with 70 wt. % nitric acid (3.77 mL) for 18 hours at room temperature in a shaking apparatus resulted in the formation of the nanoporous structure by selective leaching of silver. The material was washed with a saturated aqueous solution of NaHCO₃, pure water, and acetone, successively. Drying of the material under reduced pressure gave the nanoporous gold (30.2 mg) and its composition was found to be Au₉₈Ag₂.

Oxidation of organosilanes

Acetone (1.5ml), water (0.1ml) and organosilanes (1 mmol) were added to the nanoporous gold (2mg, 1 mol%) in a micro reaction vial with balloon at room temperature. The mixture was stirred for 1 h at room temperature. The catalyst was removed and the reaction mixture was then concentrated under reduced pressure to give a crude material. The chemical yield of product was determined by the weight and ¹H NMR. The recovered catalyst was washed with acetone and dried in vacuo, and reused.

Product Identification

The products were identified by NMR and GC-MS. The silanes of entry 1-7 in table 1.7 were commercially available. The silane of entry 8 in table 1.7 was prepared according to the literature.¹ The silanols of entry 1-8 in table 1.7 were identified by comparison of their ¹H and ¹³C NMR signals with the literature data.² The generated gas in the oxidation reaction of organosilanes was identified to be hydrogen gas by MS.

Reference

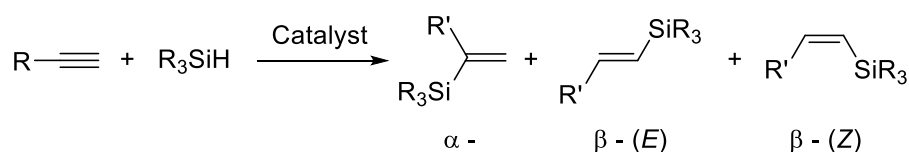
1. M. Lee, S. Ko, S. Chang, *J. Am. Chem. Soc.* **2000**, *122*, 12011
2. a) Y. Lee, D. Seomoon, S. Kim, H. Han, S. Chang, P. H. Lee, *J. Org. Chem.* **2004**, *69*, 1741
b) H. Tan, A. Yoshikawa, M. S. Gordon, J. H. Espenson, *Organometallics* **1999**, *18*, 4753
c) W. Adam, C. M. Mitchell, C. R. Saha-Moïller, O. Weichold, *J. Am. Chem. Soc.* **1999**, *121*, 2097
d) B. P. S. Chauhan, A. Sarkar, M. Chauhan, A. Roka, *Appl. Organometal. Chem.* **2009**, *23*, 385
e) K. Hirabayashi, E. Takahisa, Y. Nishihara, A. Mori, T. Hiyama, *Bull. Chem. Soc. Jpn.* **1998**, *71*, 2409

Section 2

Nanoporous gold catalyzed selective hydrosilylation reaction of alkynes

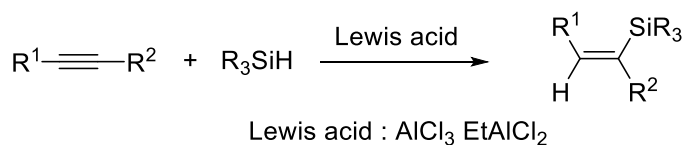
1, Introduction

The hydrosilylation of acetylenic compounds is powerful synthetic method for vinylsilane compounds,¹ which are synthetically versatile organosilicon reagents in organic synthesis.² Since three isomeric products, α , β -(*E*)-, and β -(*Z*)-isomers, can possibly be formed with terminal alkynes (Scheme 1.5), the control of region- and stereo-selectivity in this process is highly desirable for selective preparation of these vinylsilane compounds.



Scheme 1.5 Addition of organosilanes to alkyne

Generally, the selectivity is mainly affected by the nature of catalysts, alkynes, hydrosilanes, and reaction conditions. We have previously reported the selective *trans*-hydrosilylation with Lewis acid catalysts, such as AlCl_3 and EtAlCl_2 , leading to the β -(*Z*)-product exclusively.³



Scheme 1.6 Trans-hydrosilylation of organosilanes to alkyne

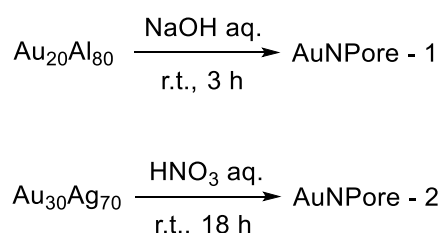
On the other hand, most of the reactions with homogeneous and heterogeneous transition metal catalysts, such as Pt, Co, Ni, and Pd, proceed in a *cis*-fashion stereo-selectively.⁴ But they often gave low regioselectivity between α , and β -(*E*)-products. I am

particularly focusing on the development of heterogeneous green catalysis because a heterogeneous catalytic system has many advantages compared to the homogeneous one, such as easy separation of catalyst from the reaction mixture, easy recycling, and enhanced stability.^{5, 6} Recently, supported-gold nanoparticles have emerged as efficient catalysts with considerable synthetic potential for many types of molecular transformations.⁷ The hydrosilylation also proceeded with these catalysts, but they often have some drawbacks, such as formation of side-products, low substrate generality, and low selectivity.⁸ A thin gold film on the surface of glass capillaries also exhibits the activity for this reaction in a continuous-flow reactor, for which cumbersome microwave irradiation is necessary.⁹

In last section, I was successful in using a monolithic nanoporous gold materials AuNPore as an effective unsupported catalyst for some molecular transformations.^{10, 11} In this section, I report that the AuNPore, fabricated from an Au-Al alloy, is an effective green catalyst for hydrosilylation of terminal alkynes, leading to β -(*E*)-products with high region- and stereo selectivities.¹²

2, Result and discussion

The requisite nanoporous gold materials were fabricated from two kinds of alloys, AuAl and AuAg. The selective removal of aluminum from an Au₂₀Al₈₀ alloy ribbon was conducted with 5 M sodium hydroxide to obtain AuNPore-1.¹³ On the other hand, AuNPore-2 was fabricated from a Au₃₀Ag₇₀ alloy thin film with 70% HNO₃ (same as AuNPore in section 1).¹⁴



Scheme 1.7 Fabrication of AuNPore-1 and AuNPore-2

The scanning electron microscopy (SEM) study revealed that both materials exhibited an open bicontinuous interpenetrating ligament channel structure with a length scale of 10 to 30 nm (Figure 1.8). The energy dispersive X-ray analysis (EDX) spectra showed

that small amount of less noble metals aluminum and silver, remained, respectively.

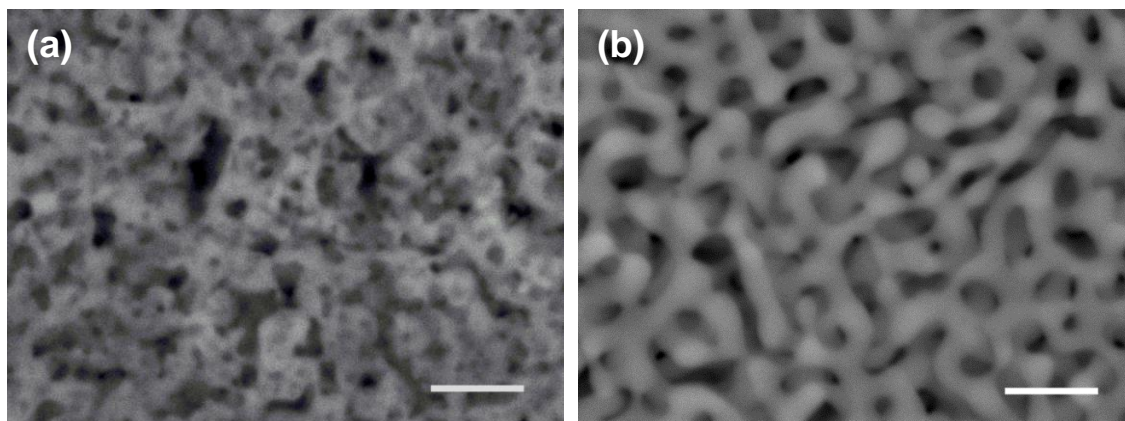
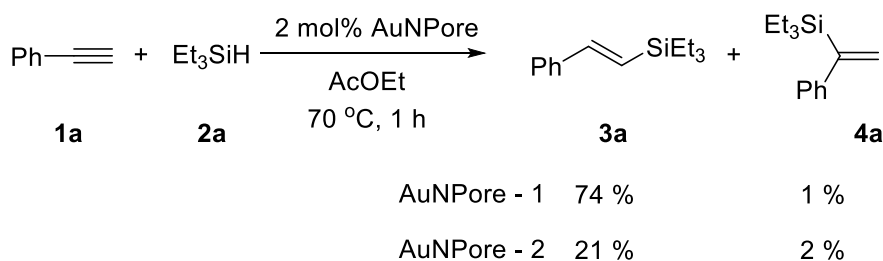


Figure 1.8 SEM image of AuNPore-1 (a) and AuNPore-2 (b)

The reaction proceeded smoothly with a catalytic amount of AuNPore-1, derived from the AuAl alloy, at 70 °C for 1 h, and gave the β -(*E*)-products in 74% yield selectively and small amount of α -isomer was produced. In contrast, the chemical yield of **3a** dramatically decreased to 21% when AuNPore-2 was used.



Scheme 1.8 Effect of AuNPore catalyst

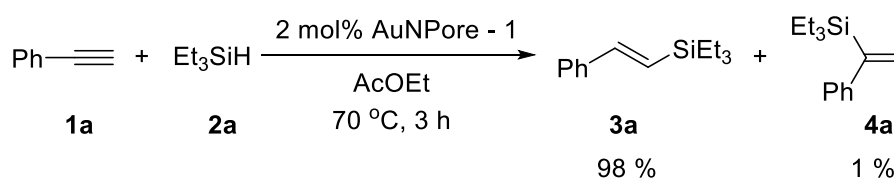
The effect of solvent is summarized in table 1.2. Besides AcOEt, 1,4-dioxane and CH₃CN are suitable solvent for this reaction (entries 2 and 3), but less polar solvents, such as (CH₂Cl)₂ and toluene, were less effective for this reaction (entries 4 and 5)

$\text{Ph}-\text{C}\equiv\text{C}-\text{H}$	+	Et_3SiH	$\xrightarrow[\text{Solvent}]{2 \text{ mol\% AuNPore - 1}}$	$\text{Ph}-\text{CH}=\text{CH}-\text{SiEt}_3$	+	$\text{Ph}-\text{C}(\text{SiEt}_3)=\text{CH}_2$
1a		2a	70 °C, 1 h	3a		4a

Entry	Solvent	Time [h]	Yield of 3a [%]	Yield of 4a [%]
1	AcOEt	1	74	1
2	Dioxane	1	66	1
3	CH ₃ CN	1	55	1
4	(CH ₂ Cl) ₂	1	48	1
5	Toluene	1	43	1

Table 1.2 Effect of solvent

Finally, optimization experiments revealed that the chemical yield of **3a** increased up to 98% when the reaction was conducted in AcOEt for 3 h (Scheme 1.9).



Scheme 1.9 Hydrosilylation reaction by AuNPore

Further studies were conducted focusing on the difference in the catalytic activity between AuNPore-1 and AuNPore-2. The specific surface area (SSA) was electrochemically measured as shown in Figure 1.9.

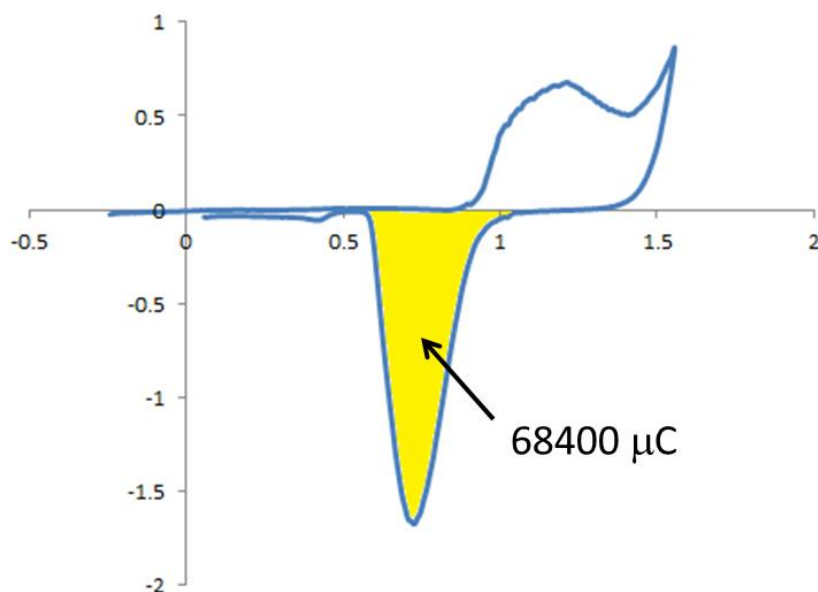
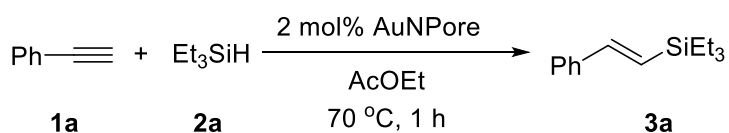


Figure 1.9 CV analysis of AuNPore-1

The CV analysis of AuNPore-1 is representative; The amount of reduction charge corresponding to the shaded region in Figure 1.9 was obtained by integrating the charge passed in the surface oxide stripping reaction recorded for AuNPore-1 (1.47 mg), which was marked in the figure. The electrochemically active surface area of the nanoporous gold is $68400 / 222 \cdot 10^4/2 = 1.54 \cdot 10^{-2}$ (m²) where $2.22 \cdot 10^4 \mu\text{C m}^{-2}$ is the gold's conversion factor.

Hence, the specific surface area was calculated to be $1.54 \cdot 10^{-2} / 1.47 \cdot 10^{-3} = 10.5$ m²/g.

The catalytic TOF was calculated and summarized in next scheme. Obviously, AuNPore-1 has a higher TOF than AuNPore-2.



Entry	Catalysts	Composition	SSA [m ² /g]	Yield of 3a [%]	TOF [h ⁻¹]
1	AuNPore - 1	Au ₉₆ Al ₄	10.5	74	757
2	AuNPore - 2	Au ₉₈ Ag ₂	12.0	21	189

Table 1.3 TOF of nanoporous golds for hydrosilylation reaction

One might think that the fabrication process of AuNPore-2 with HNO₃ would deactivate the materials. To check the effect of HNO₃, AuNPore-3 is fabricated like scheme 1.9.



Scheme 1.9 Fabrication of AuNPore-3

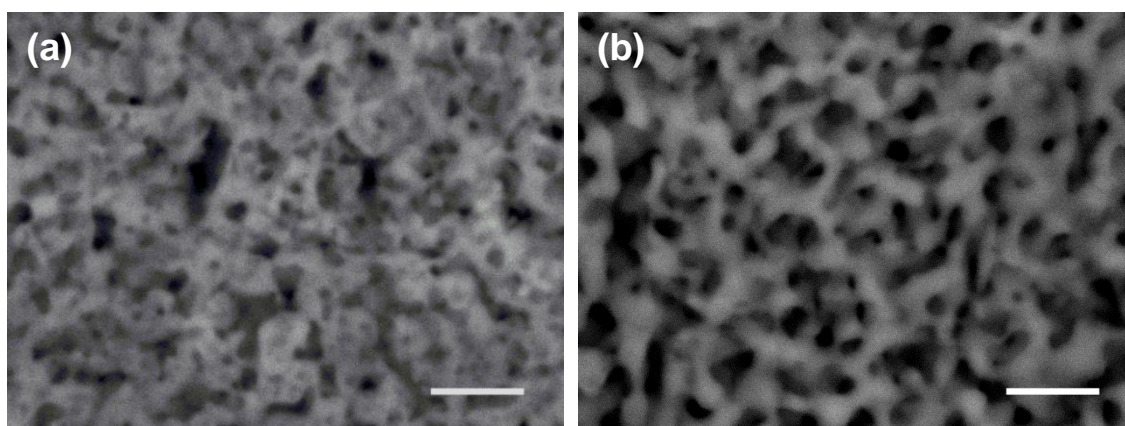
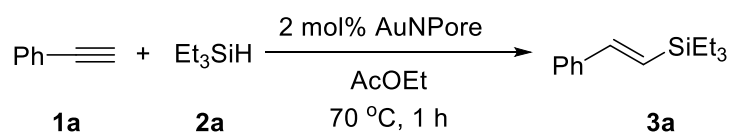


Figure 1.10 SEM image of of AuNPore-1 (a) and AuNPore-3 (b)

However, the catalytic activity of AuNPore-1 did not change upon treatment with 70% HNO₃ although the surface area of the resulting AuNPore slightly decreased as reported previously (Table 1.4).¹⁵



Entry	Catalysts	Composition	SSA [m ² /g]	Yield of 3a [%]	TOF [h ⁻¹]
1	AuNPore - 1	Au ₉₆ Al ₄	10.5	74	757
2	AuNPore - 2	Au ₉₈ Ag ₂	12.0	21	189
3	AuNPore - 3	Au ₉₈ Al ₂	8.4	62	789

Table 1.4 TOF of AuNPores for hydrosilylation reaction

These results suggested that two plausible synergistic effects generated by the residual metals should be considered. One is the activation effect by aluminum, and the other is the deactivation effect by silver.

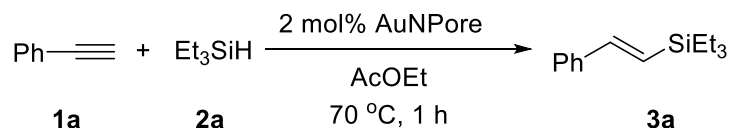
Then, we next fabricated new nanoporous gold catalysts, including both aluminum and silver, from the Au₁₉Ag₁Al₈₀ alloy ribbon. The chemical etching was carried out with 5 M sodiumhydroxide of the selective removal of aluminum to obtain Au₉₃Ag₃Al₄ (AuNPore-4). In addition, by the acid etching silver decreased AuNPore-5 was fabricated from AuNPore-4.



Scheme 1.9 Fabrication of AuNPore-4 and AuNPore-5

Figure 1.11 SEM image of AuNPore-4 (a) and AuNPore-5 (b)

I found that the catalytic activity of AuNPore-4 was quite low and **3a** was produced in only 2% yield. In contrast, after immersion of AuNPore-4 in HNO₃, the resulting AuNPore-5, having lower amount of silver, exhibited comparable catalytic activity of AuNPore-2. At the same time, this result also indicated that aluminum had no special activation effect on this reaction.



Entry	Catalysts	Composition	SSA [m ² /g]	Yield of 3a [%]	TOF [h ⁻¹]
1	AuNPore - 1	Au ₉₆ Al ₄	10.5	74	757
2	AuNPore - 2	Au ₉₈ Ag ₂	12.0	21	189
3	AuNPore - 3	Au ₉₈ Al ₂	8.4	62	789
4	AuNPore - 4	Au ₉₃ Ag ₃ Al ₄	11.3	2	19
5	AuNPore - 5	Au ₉₆ Ag ₁ Al ₃	8.3	16	207

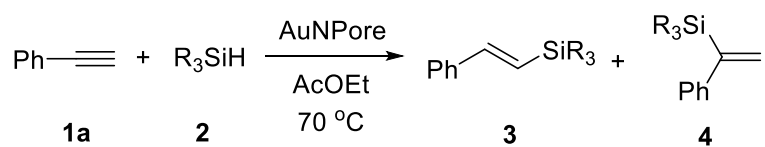
Table 1.5 TOF of AuNPores for hydrosilylation reaction

The alkyne generality was examined and the results are summarized in Table 1.6. In every cases, the reactions gave the product **3** in high yields together with less than 3% of **4**. Compared to the phenylacetylene **1a**, *p*-fluorophenylacetylene **1b** was more reactive and **3b** was obtained in 97% yield in 2 h. On the other hand, the reaction of *p*-methoxyphenylacetylene **1c** needed longer reaction times. These result clearly showed that the electron-withdrawing groups on the phenyl group promoted the present reaction. Not only aromatic alkynes but also aliphatic alkynes are suitable for this reaction system.

$ \begin{array}{c} \text{R}-\text{C}\equiv\text{C} + \text{Et}_3\text{SiH} \xrightarrow[\text{AcOEt, 70 }^\circ\text{C}]{2 \text{ mol\% AuNPore}} \text{R}-\text{CH}=\text{CH}-\text{SiEt}_3 + \begin{array}{c} \text{Et}_3\text{Si} \\ \\ \text{Ph} \end{array} \text{C}=\text{C} \\ \text{1} \qquad \text{2a} \qquad \qquad \qquad \text{3} \qquad \qquad \qquad \text{4} \end{array} $					
Entry	R		Time [h]	Yield of 3 [%]	Yield of 4 [%]
1	C ₆ H ₅	1a	3	98	1
2	<i>p</i> -FC ₆ H ₄	1b	2	97	2
3	<i>p</i> -MeOC ₆ H ₄	1c	6	97	2
4	C ₆ H ₁₃	1d	3	99	2
5	PhCH ₂	1e	3	97	1
6	<i>c</i> -C ₆ H ₁₁	1f	3	97	1

Table 1.6 Scope of the hydrosilylation reaction

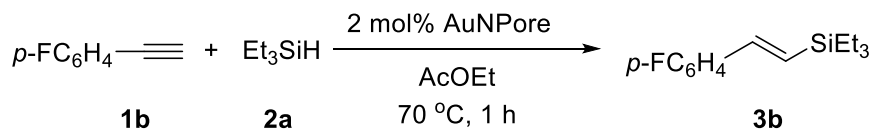
The hydrosilane generality was examined and the results are summarized in Table 1.7. Besides Et₃SiH, other hydrosilanes were available. Even with sterically bulky (iPr)₃SiH the reaction proceeded to give the corresponding vinylsilane in 80% yield although increased loading amounts of catalyst and longer reaction time were required.



Entry	R ₃ SiH		Cat. [mol%]	Time [h]	Yield of 3 [%]	Yield of 4 [%]
1	Et ₃ SiH	2a	2	3	98	1
2	PhMe ₂ SiH	2b	2	6	96	3
3	(EtO) ₃ SiH	2c	5	12	85	3
4	Bu ₃ SiH	2d	10	12	98	2
5	(i-Pr) ₃ SiH	2e	20	18	80	2

Table 1.7 Scope of the hydrosilylation reaction

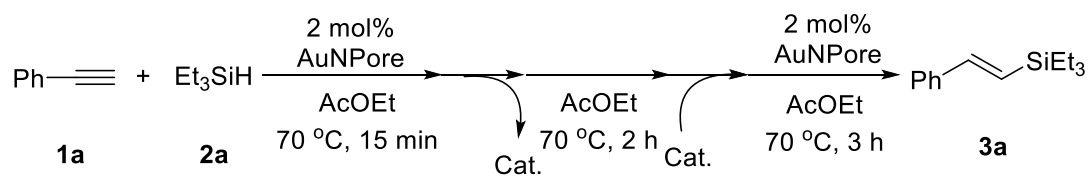
The catalyst can be recovered easily by tweezers and any cumbersome separation procedures, such as filtration and centrifugation, are not required. We conducted the reaction of *p*-fluorophenylacetylene several times with re recovered catalyst, but no significant loss of the catalytic activity was observed even after 5 times (Table 1.8).



Entry	Catalyst	Yield of 3b [%]
1	fresh	97
2	reuse 1	98
3	reuse 2	97
4	reuse 3	97
5	reuse 4	97

Table 1.8 Reusing test

We next investigated the leaching test. The hydrosilylation of triethylsilanes to phenylacetylene was carried out for 15 min under the standard conditions, and product was produced in 22% yield at this time. Then the catalyst was removed from the reaction vessel. Even after stirring for 2 h in the absence of the catalyst, further generation of product was not detected at all. The reaction restarted when the removed catalyst was put back into the mixture, and finally product **3a** was obtained in 96% yield (Figure 1.12).



Scheme 1.10 Leaching test

Figure 1.12 Result of leaching test

Furthermore, leaching of the gold into the reaction mixture was not detected by inductively coupled plasma analysis (ICP). These results clearly indicated that the current transformation was really heterogeneous.

In conclusion, we have disclosed that the AuNPore exhibited a remarkable catalytic activity in the hydrosilylation of alkynes as a non-supported nanostructured catalyst. The reaction does not need any additives, such as bases, stabilizers, and ligands, as well as any cumbersome work-up procedures like filtration or centrifugation.

3. Reference

1. a) B. Marciniec, *Silicon Chem.*, **2002**, *1*, 155
b) B. M. Trost, Z. T. Ball, *Synthesis*, **2005**, 853
2. a) E. Langkopf, D. Schinzer, *Chem. Rev.*, **1995**, *95*, 1375
b) D. S. W. Lim, E. A. Anderson, *Synthesis*, **2012**, 983.
3. a) N. Asao, T. Sudo, Y. Yamamoto, *J. Org. Chem.*, **1996**, *61*, 7654
b) T. Sudo, N. Asao, V. Gevorgyan, Y. Yamamoto, *J. Org. Chem.*, **1999**, *64*, 2494
c) T. Sudo, N. Asao, Y. Yamamoto, *J. Org. Chem.*, **2000**, *65*, 8919
- 4) A. K. Roy, *Adv. Organomet. Chem.*, **2008**, *55*, 1
- 5) K. Kaneda, K. Ebitani, T. Mizugaki, K. Mori, *Bull. Chem. Soc. Jpn.*, **2006**, *79*, 981
- 6) a) P. Boudjouk, B. H. Han, J. R. Jacobsen, B. J. Hauck, *J. Chem. Soc., Chem. Commun.*, **1991**, 1424
b) C. Polizzi, A. M. Caporusso, G. Vitulli, P. Salvatori, M. Pasero, *J. Mol. Catal.*, **1994**, *91*, 83
c) M. A. Brook, H. A. Ketelson, F. J. LaRonde, R. Pelton, *Inorg. Chim. Acta*, **1997**, *264*, 125
d) Z. M. Michalska, K. Strzelec, J. W. Sobczak, *J. Mol. Catal. A: Chem.*, **2000**, *156*, 91
e) R. Jiménez, J. M. Lopez, J. Cervantes, *Can. J. Chem.*, **2000**, *78*, 1491
f) M. Chauhan, B. J. Hauck, L. P. Keller, P. Boudjouk, *J. Organomet. Chem.*, **2002**, *645*, 1
g) M. Okamoto, H. Kiya, H. Yamashita, E. Suzuki, *Chem. Commun.*, **2002**, 1634
h) R. Jiménez, J. M. Martínez Rosales, J. Cervantes, *Can. J. Chem.*, **2003**, *81*, 1370
i) H. Hagio, M. Sugiura, S. Kobayashi, *Synlett*, **2005**, 813
j) E. Ramírez-Oliva, A. Hernández, J. M. Martínez-Rosales, A. Aguilar-Elguezabal, G. Herrera-Pérez, J. Cervantes, *ARKIVOC*, **2006**, V, 126
k) A. Hamze, O. Provot, J.-D. Brion, M. Alami, *Synthesis*, **2007**, 2025
l) M. Okamoto, H. Kiya, A. Matsumura, E. Suzuki, *Catal. Lett.*, **2008**, *123*, 72
m) H.-H. Shih, D. Williams, N. H. Mack, H.-L. Wang, *Macromolecules*, **2009**, *42*, 14
n) F. Alonso, R. Buitrago, Y. Moglie, J. Ruiz-Martínez, A. Sepúlveda-Escribano, M. Yus, *J. Organomet. Chem.*, **2011**, *696*, 368

- o) R. Cano, M. Yus, D. J. Ramón, *ACS Catal.*, **2012**, *2*, 1070
7. a) A. Corma, A. Leyva-Pérez, M. J. Sabater, *Chem. Rev.*, **2011**, *111*, 1657
 b) Y. Zhang, X. Cui, F. Shi, Y. Deng, *Chem. Rev.*, **2012**, *112*, 2467
 c) M. Stratakis, H. Garcia, *Chem. Rev.*, **2012**, *112*, 4469.
8. a) A. M. Caporusso, L. A. Aronica, E. Schiavi, G. Martra, G. Vitulli, P. Salvadori, *J. Organomet. Chem.*, **2005**, *690*, 1063
 b) A. Corma, C. González-Arellano, M. Iglesias, F. Sánchez, *Angew. Chem., Int. Ed.*, **2007**, *46*, 7820
 c) L. A. Aronica, E. Schiavi, C. Evangelisti, A. M. Caporusso, P. Salvadori, G. Vitulli, L. Bertinetti, G. Martra, *J. Catal.*, **2009**, *266*, 250
 d) A. Psyllaki, I. N. Lykakis, M. Stratakis, *Tetrahedron*, **2012**, *68*, 8724
9. G. Shore, M. G. Organ, *Chem. Eur. J.*, **2008**, *14*, 9641.
10. a) N. Asao, Y. Ishikawa, N. Hatakeyama, M. Bateer, Y. Yamamoto, M. Chen, W. Zhang, A. Inoue, *Angew. Chem., Int. Ed.*, **2010**, *49*, 10093
 b) N. Asao, N. Hatakeyama, Menggenbateer, T. Minato, E. Ito, M. Hara, Y. Kim, Y. Yamamoto, M. Chen, W. Zhang, A. Inoue, *Chem. Commun.*, **2012**, *48*, 4540
 c) N. Asao, Menggenbateer, Y. Seya, Y. Yamamoto, M. Chen, W. Zhang, A. Inoue, *Synlett*, **2012**, 66
 d) M. Yan, T. Jin, Y. Ishikawa, T. Minato, T. Fujita, L.-Y. Chen, M. Bao, N. Asao, M.-W. Chen, Y. Yamamoto, *J. Am. Chem. Soc.*, **2012**, *134*, 17536
11. N. Asao, T. Jin, S. Tanaka, Y. Yamamoto, *Pure Appl. Chem.*, **2012**, *84*, 1771
12. T. Fujita, P. F. Guan, K. McKenna, X. Y. Lang, A. Hirata, L. Zhang, T. Tokunaga, S. Arai, Y. Yamamoto, N. Tanaka, Y. Ishikawa, N. Asao, Y. Yamamoto, M. W. Chen, *Nat. Mater.*, **2012**, *11*, 775
13. Z. Zhang, Y. Wang, Z. Qi, W. Zhang, J. Qin, J. Frenzel, *J. Phys. Chem. C*, **2009**, *113*, 12629.
14. a) A. J. Forty, *Nature*, **1979**, *282*, 597
 b) J. Erlebacher, M. Aziz, A. Karma, *Nature*, **2001**, *410*, 450

15 Y. Ding, Y.-J. Kim, J. Erlebacher, *Adv. Mater.*, **2004**, *16*, 1897

4. Experimental section

General information

For thin layer chromatography (TLC) analysis throughout this work, Merck pre coated TLC plates (silica gel 60 GF254, 0.25 mm) were used. The products were purified by flash column chromatography on silica gel 60 (Merck, 230-400 mesh). GC-MS analysis was performed on an Agilent 6890N GC interfaced to an Agilent 5973 mass-selective detector (30 m x 0.25 mm capillary column, HP-5MS). Scanning electron microscope (SEM) observations were carried out using JEOL JSM-7800F instruments operated at accelerating voltages of 15 kV, respectively. EDX analysis was carried out using Oxford X-max50 with JEOL JSM-7800F operated at an accelerating voltage of 15 kV. The CV measurements were carried out in a conventional three-electrode cell at ambient temperature by using an Iviumstat electrochemical analyzer (Ivium Technology). Nanoporous gold fixed to glassy carbon electrode with nafion was employed as the working electrodes, and a saturated calomel electrode and a Pt plate were used as the reference and counter electrodes, respectively. ICP analysis was performed on Shimadzu ICPS-7510 equipment.

Fabrication of Nanoporous Gold Catalyst

AuNPore-1 ($\text{Au}_{96}\text{Al}_4$): Au (99.99%) and Al (99.99%) were melted with electric arc-melting furnace under Ar atmosphere to form Au/Al alloy (20:80, in at. %), which was manufactured to thickness of 40 μm ribbon by melt spinning method. Treatment of the resulting ribbon with 20 wt. % aqueous sodium hydroxide for 3h at room temperature resulted in the formation of the nanoporous structure by selective leaching of aluminum. The material was washed with pure water, and acetone, successively. Drying of the material under reduced pressure gave the nanoporous gold (AuAl) and its composition was found to be $\text{Au}_{96}\text{Al}_4$ by EDX analysis.

AuNPore-2 ($\text{Au}_{98}\text{Ag}_2$): Au (99.99%) and Ag (99.99%) were melted with electric arc-melting furnace under Ar atmosphere to form Au/Ag alloy (30:70, in at. %), which was rolled down to thickness of 40 μm . The foil was cut into small pieces (2 x 5 mm square). Treatment of the resulting several chips with 70 wt. % nitric acid for 18 hours at room temperature resulted in the formation of the nanoporous structure by selective leaching of silver. The material was washed with pure water, and acetone, successively. Drying of the material under reduced pressure gave the nanoporous gold (AuAg) and its composition was found to be $\text{Au}_{98}\text{Ag}_2$ by EDX analysis.

AuNPore-3 ($\text{Au}_{98}\text{Al}_2$): AuNPore-1 was treated with 70 wt. % nitric acid for 1 hour at

room temperature. The material was washed with pure water and acetone, successively. The material was dried under reduced pressure and its composition was found to be Au₉₈Al₂.

AuNPore-4 (Au₉₃Ag₃Al₄): Au (99.99%), Ag (99.99%) and Al (99.99%) were melted with electric arc-melting furnace under Ar atmosphere to form Au:Ag:Al alloy (19:1:80, in at. %), which was manufactured to thickness of 40 μm ribbon by melt spinning method. Treatment of the resulting ribbon with 20 wt. % aqueous sodium hydroxide for 3h at room temperature resulted in the formation of the nanoporous structure by selective leaching of aluminum. The material was washed with pure water, and acetone, successively. Drying of the material under reduced pressure gave the nanoporous gold (AuAgAl) and its composition was found to be Au₉₃Ag₃Al₄ by EDX analysis.

AuNPore-5 (Au₉₆Ag₁Al₃): AuNPore-4 was treated with 70 wt. % nitric acid for 1 hour at room temperature. The material was washed with pure water and acetone, successively. The material was dried under reduced pressure and its composition was found to be Au₉₆Ag₁Al₃.

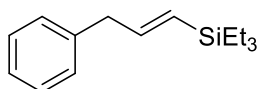
Hydrosilylation reaction

Ethylacetate (3 ml), alkyne (1 mmol) and organosilanes (1.5 mmol) were added to the nanoporous gold (4mg, 2 mol%) in a micro reaction vial at room temperature. The mixture was heated to 70 °C and stirred for 3 h at room temperature. The catalyst was removed and the reaction mixture was then concentrated under reduced pressure to give a crude material. The chemical yield of product was determined by ¹H NMR using *p*-xylene as internal standard. The recovered catalyst was washed with acetone and dried in vacuo, and reused.

Characterization Data

Spectral data of products are consistent with the literature data¹

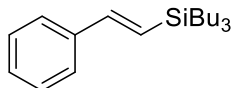
(*E*)-Triethyl(3-phenylprop-1-enyl)silane



Colorless oil; IR (neat, cm⁻¹): 2941, 2909, 2873; ¹H NMR (400 MHz, CDCl₃) δ 7.35-7.18 (m, 5H), 6.19 (dt, *J* = 18.4 Hz, 6.4 Hz, 1H), 5.68 (dt, *J* = 18.4Hz, 1.6Hz, 1H), 3.50 (d, *J* = 6.4 Hz, 2H), 0.96 (t, *J* = 7.6Hz, 9H), 0.59 (q, *J* = 7.6Hz, 6H) ¹³C NMR (100 MHz, CDCl₃) δ 146.3, 140.1, 128.6, 128.3, 127.7, 125.9, 43.6, 7.5, 3.6; HRMS (EI) calcd for C₁₅H₂₄Si, 232.1647; found 232.1644. Minor α product was observed: ¹H NMR (300 MHz CDCl₃):

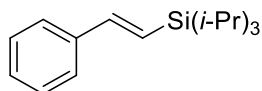
δ 5.52-5.54 (m, 1H), 5.43-5.45 (m, 1H)

(*E*)-Tributyl(styryl)silane



Colorless oil; IR (neat, cm^{-1}): 2955, 2918, 2870, 2855; ^1H NMR (400 MHz, CDCl_3) δ 7.48-7.22 (m, 5H), 6.89 (d, $J = 19.2$ Hz, 1H), 6.45 (d, $J = 19.2$, 1H), 1.40-1.29 (m, 12H), 0.92 (t, $J = 2.8$, 9H), 0.72-0.64 (m, 6H) ^{13}C NMR (100 MHz, CDCl_3) δ 144.3, 138.5, 128.4, 127.8, 126.9, 126.2, 26.8, 26.2, 13.9, 12.4; HRMS (EI) calcd for $\text{C}_{20}\text{H}_{34}\text{Si}$, 302.2430; found 302.2426. Minor α product was observed: ^1H NMR (300 MHz CDCl_3): δ 5.86 (d, $J = 2.8$ Hz, 1H), 5.58 (d, $J = 2.8$ Hz, 1H)

(*E*)-Triisopropyl(styryl)silane



Colorless oil; IR (neat, cm^{-1}): 3060, 3027, 2952, 2909, 2873; ^1H NMR (400 MHz, CDCl_3) δ 7.50-7.22 (m, 5H), 6.95 (d, $J = 19.2$ Hz, 1H), 6.41 (d, $J = 19.2$), 1.14-1.09 (m, 21H) ^{13}C NMR (100 MHz, CDCl_3) δ 145.5, 138.6, 128.4, 127.8, 126.2, 123.9, 18.8, 11.1; HRMS (EI) calcd for $\text{C}_{17}\text{H}_{28}\text{Si}$, 260.1960; found 260.1963. Minor α product was observed: ^1H NMR (300 MHz CDCl_3): δ 5.89 (d, $J = 2.8$ Hz, 1H), 5.66 (d, $J = 2.8$ Hz, 1H)

Reference

- a) A. Battace, T. Zair, H. Doucet and M. Santelli, *J. Organomet. Chem.*, **2005**, 690, 3790.
- b) M. R. Chaulagain, G. M. Mahandru and J. Montgomery, *Tetrahedron*, **2006**, 62, 7560.
- c) C. G. Jun and R. H. Crabtree, *J. Organomet. Chem.*, **1993**, 447, 177.
- d) A. Psyllaki, I. N. Lykakis and M. Stratakis, *Tetrahedron*, **2012**, 68, 8724.

Chapter 2

Fabrication of ultrafine titanate nanowires
with extraordinary ion-exchange property

1, Introduction

The decontamination of radiation-tainted water caused by a nuclear accident is an emergent issue,¹⁻³ Sodium titanate has gained attention because radioactive cations and adsorbed radioactive ions can be immobilized, leading to safe disposal.⁴⁻²⁵ A variety of titanate nanostructures have been produced by hydrothermal, sol-gel, and other methods.⁴⁻²⁵ However, the product sized relatively larger because these methods involve high-temperature treatments that lead to crystal growth. Herein, we report a new synthetic method involving a non-thermal process that allows for the formation of ultrafine nanowires. The key to produce such nanowires originates from the simultaneous aluminum leaching and titanium oxidation of Ti-Al alloy ribbons in alkaline medium at room temperature.

2, Result and discussion

The requisite TiAl alloy ribbon were produced from the mother alloy ingot with a nominal composition of $\text{Ti}_6\text{Al}_{94}$ by single-roller melt spinning method (Figure 2.1).

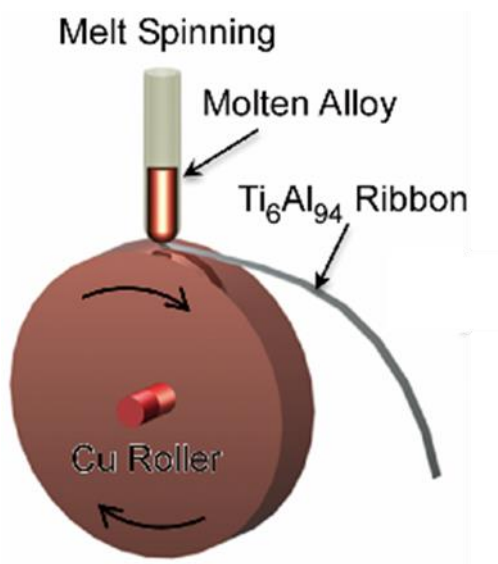


Figure 2.1 Image of melt spinning

A bright-field magnified transmission electron microscopy (TEM) image of the ribbon sample reveals that the TiAl_3 intermetallic compound nanocrystals (appearing

granularly dark under moiré fringe contrast) with the diameter of approximately 50 nm are distributed uniformly in the Al matrix.

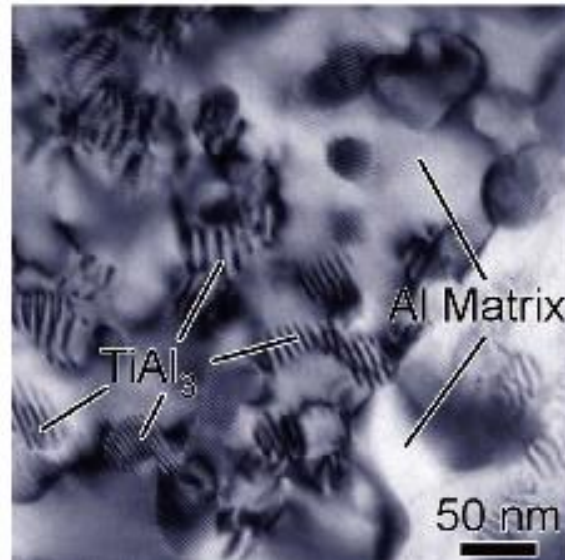


Figure 2.2 TEM image of obtained melt spun ribbon

The XRD profile shows that TiAl₃ with energetically stable tetragonal D0₂₂-type and metastable cubic L1₂ types structure can be assigned in addition to fcc Al (Figure 2.3).²⁶

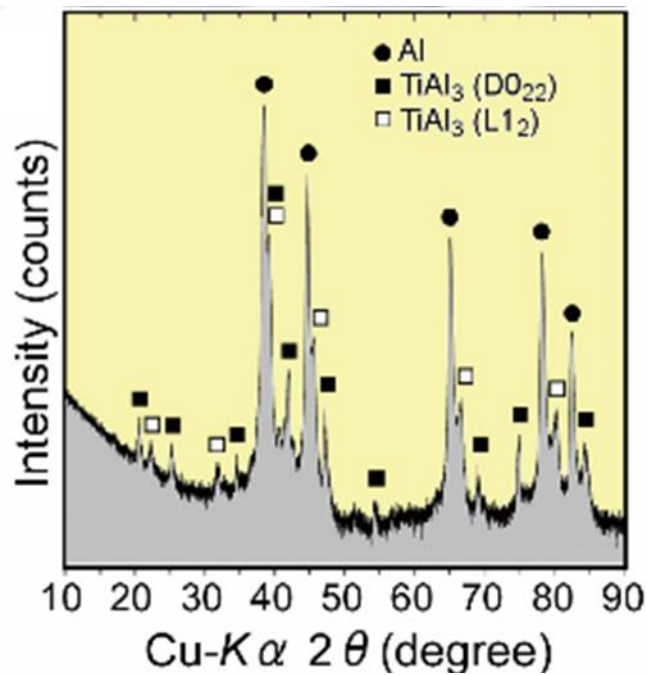
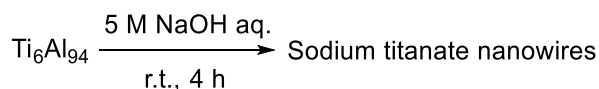


Figure 2.3 XRD of obtained melt spun ribbon

These results are in good agreement with the TEM observation and the prediction of phase separation for TiAl_3 and Al in the $\text{Ti}_6\text{Al}_{94}$ composition alloy.²⁷ Room-temperature treatment of the $\text{Ti}_6\text{Al}_{94}$ ribbon in 5 M sodium hydroxide aqueous solution resulted in a whitish turbidness along with evolution of hydrogen gas, as depicted in Figure 2.4.



Scheme 2.1 Fabrication of sodium titanate nanowires

Al Leaching & Ti Oxidizing

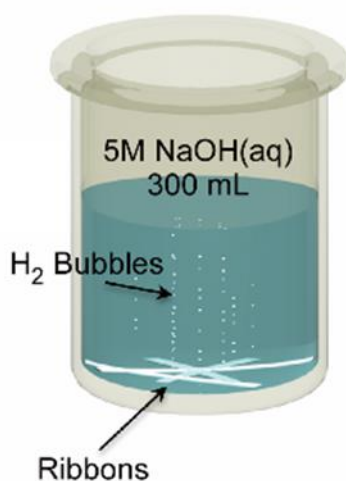


Figure 2.4 Image of dealloying

Finally, sodium titanate nanowires were obtained after the centrifugation of the turbid solution. The picture of obtained nanowires is shown in Figure 2.5. To the best of my knowledge, this is the first example of the fabrication method of metal oxide nanowires by simultaneous leaching and oxidizing process.



Figure 2.5 Picture of obtained sodium titanate nanowires

Bright-field TEM images of the ultrafine nanowires are shown in Fig. 2.6 and 2.7. Fig. 2.6 taken at lower magnification reveals that hierarchical nanostructures with diameters of a few hundred nanometers and aggregation of highly dense nanowires creates a cotton like skeletal structure with a three-dimensional network. The individual nanowires have diameters of a few nanometers with large aspect ratios (Fig. 2.7).

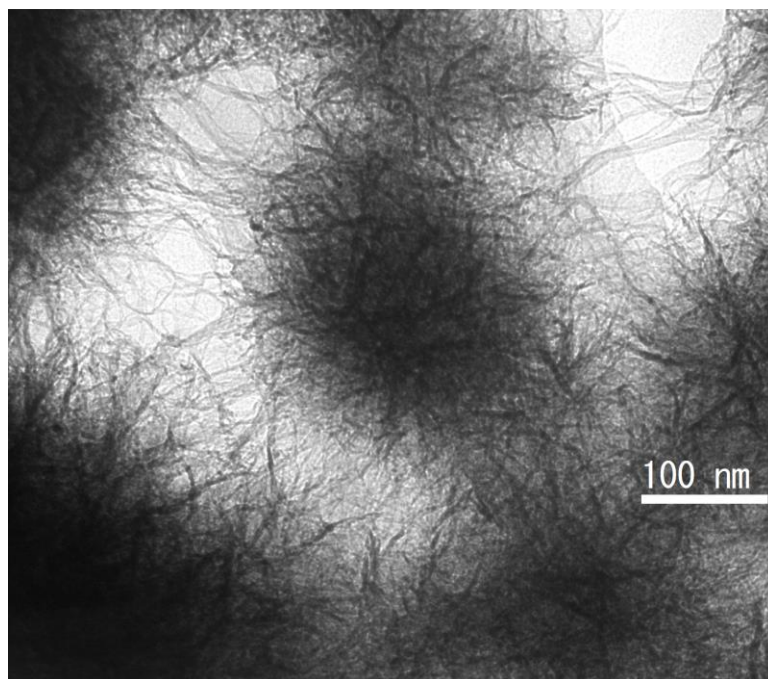


Figure 2.6 Bright field TEM image of nanowires (Low magnification)

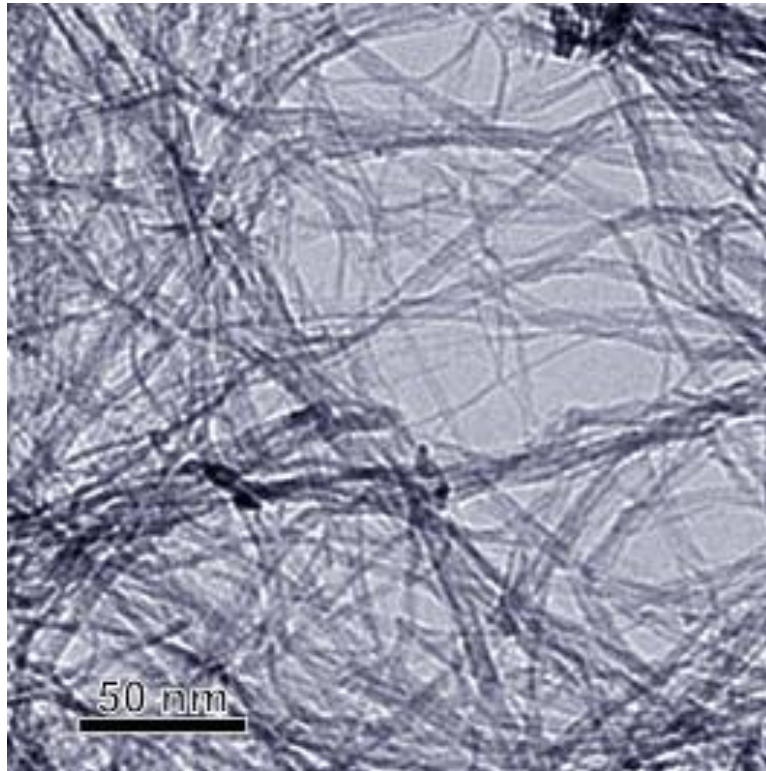


Figure 2.7 Bright field TEM image of nanowires (High magnification)

Figure 2.8 shows nano-beam diffraction patterns (NBDP) with concentric hollow rings obtained at the amorphous region, which partially exists in the nanowires and crystalline region.

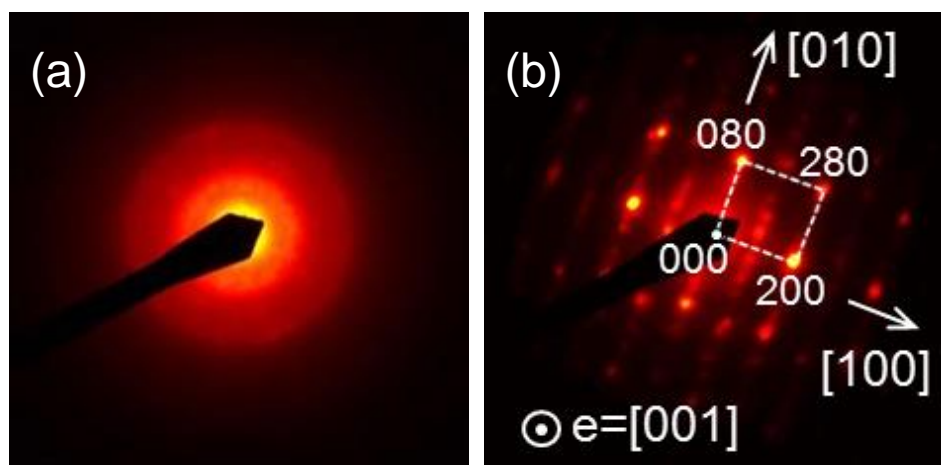


Figure 2.8 NBDP obtained from amorphous phase (a) and crystalline phase (b)

The results of the TEM-NBDP and XRD measurements (Figure 2.9) identify that the layered crystal structure with a body-centered orthorhombic unit cell possesses a sequential framework stacking of TiO_6 -octahedra layers and intercalated layers (Figure 2.10).

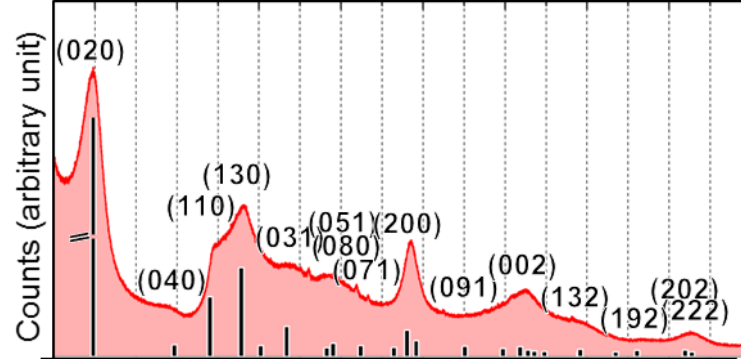


Figure 2.9 XRD of sodium titanate nanowires

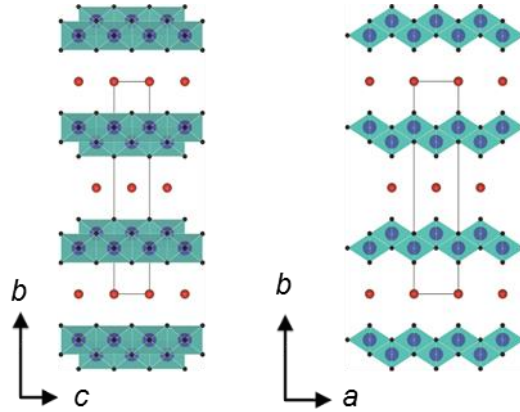


Figure 2.10 Crystalline model of sodium titanate nanowires

This structure is related to lepidocrocite and has been reported as a series of “non-stoichiometric” layered titanates with the composition $\text{A}_x\text{Ti}_{2-x/4}\text{O}_{4-x/4}$ (where A denotes alkali metal, hydrogen, or H_3O^+ molecule and \diamond denotes a vacancy).²⁸⁻³¹ The XRD pattern is obtained based on the lattice constants of $a_0 = 0.37$ nm, $b_0 = 1.82$ nm and $c_0 = 0.30$ nm. Consequently, these constants are different from those of “stoichiometric” sodium titanates of $\text{Na}_2\text{Ti}_3\text{O}_7$ and $\text{Na}_2\text{Ti}_6\text{O}_{13}$.^{32, 33} It is also evident that the NBDP diffraction obtained from the incident electron beam parallel to the $[001]$ direction shows a series of weak streaks and super lattice spot contrast along the $[010]$ direction, which corresponds to the lattice planes parallel to the TiO_6 -octahedra and intercalated layers.

Furthermore, high-resolution TEM (HRTEM) observations also reveal that the diameter of the nanowires is approximately 2 nm and the nanowires have a crystallographic tendency to grow along the $[100]$ direction parallel to the TiO_6 -octahedra and intercalated layers (Figure 2.11 and 2.12).

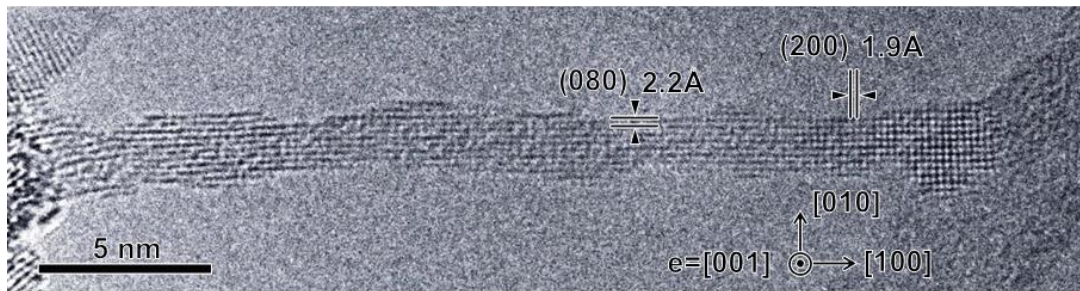


Figure 2.11 HRTEM image of sodium titanate nanowires

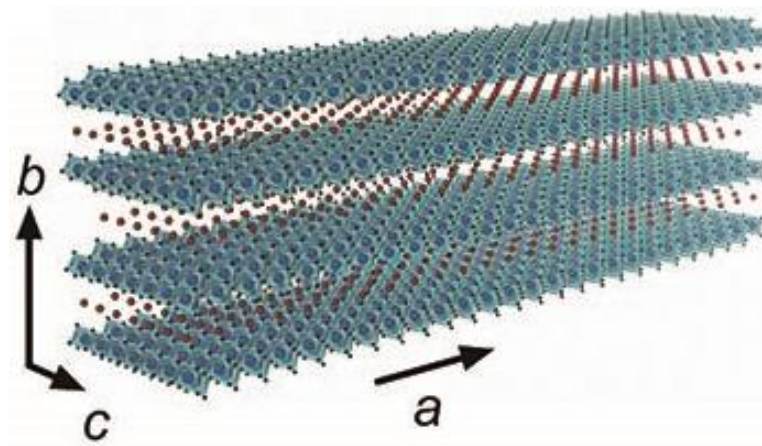


Figure 2.12 Structure model of sodium titanate nanowires

The energy dispersive X-ray spectroscopy (EDS) analysis shows that the Al is completely dissolved (Figure 2.13).

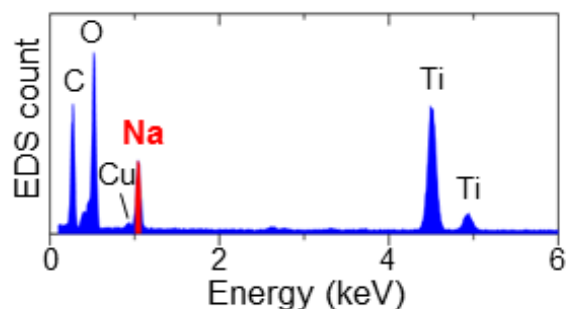


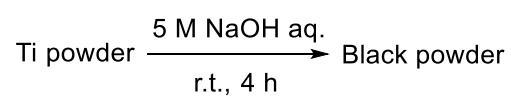
Figure 2.13 EDS result of sodium titanate nanowires

We further verified the amount of Al in the nanowires using inductively coupled plasma-mass spectrometry (ICP-MS) by dissolution of titanate nanowires in aqueous HCl because the sensitivity of ICP-MS is much higher than that of EDX. A small amount of Al was detected, but the Al intermetallic phase excluded in the titanate nanowire. The ICP-MS results also identify that the atomic ratio of Na to Ti is 0.57 ± 0.02 , which leads to $x \doteq 1$ in the $\text{Na}_x\text{Ti}_{2-x/4}\text{O}_4$ structure.

The ligaments produced by simple dealloying protocols, such as Raney nickel³⁴ and nanoporous gold,³⁵ do not achieve diameters in the low single-digit nanometers. On the basis of the weak metallic bonding, the rapid and consecutive ad-atom diffusion on the metal surface leads to self-healing and facet formation even at room temperature. In contrast, the mogul-shaped surface structures in this study are created under the kinetic limited circumstances where the diffusion length of ad-atoms is much shorter because the stronger ionic or covalent bonds in titanates.

The key to creating such ultrafine nanowires originates with a TiAl_3 nanocrystal, which is the intermetallic compound in the Al matrix included in the rapidly quenched $\text{Ti}_{60}\text{Al}_{40}$ alloy, as the shown in Figure 2.2.

To confirm this result, pure titanium powder, $\text{Ti}_{50}\text{Al}_{50}$ alloy, and $\text{Ti}_{25}\text{Al}_{75}$ alloy are treated with 5 M NaOH aqueous solution at room temperature. Although nanowires can be produced from the pure metallic titanium powder, they appear only on surface and their diameter is an order of magnitude larger (Figure 2.14 - 2.16).^{36, 37}



Scheme 2.2 Base treatment of metallic Ti

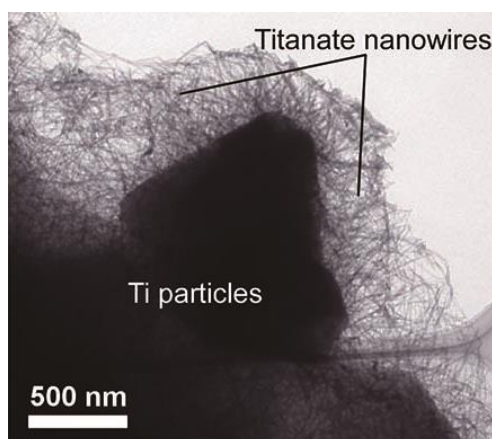


Figure 2.14 TEM image of base treated Ti (Low magnification)

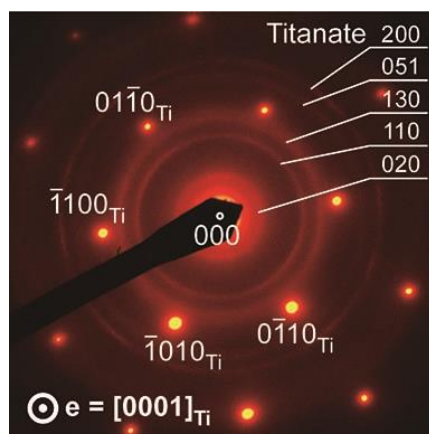


Figure 2.15 NBDP of base treated Ti

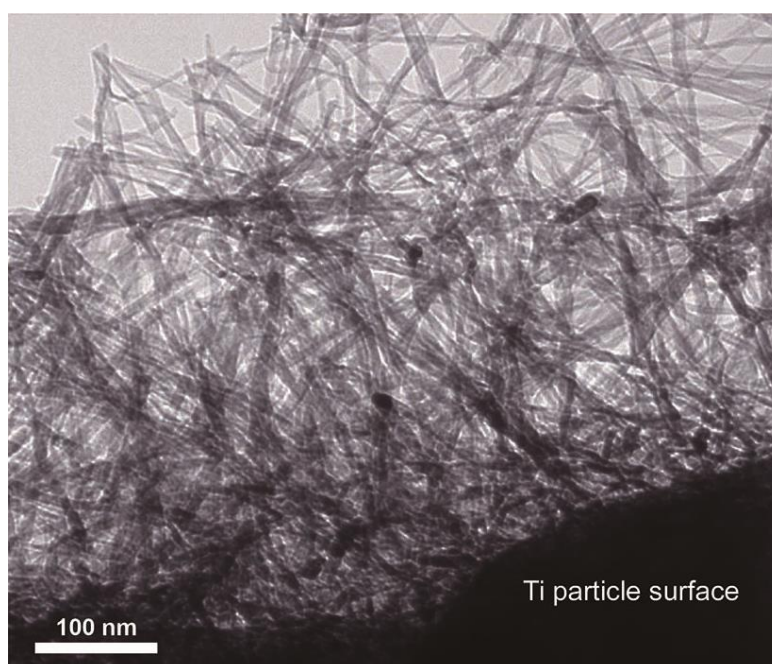
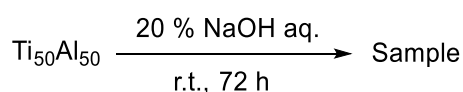


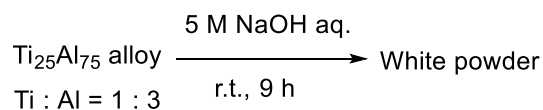
Figure 2.16 TEM image of base treated Ti (High magnification)

In the case of the $\text{Ti}_{50}\text{Al}_{50}$ alloy, which consists of a TiAl_1 phase, the Al leaching was not accomplished even after 3 days.



Scheme 2.3 Base treatment of $\text{Ti}_{50}\text{Al}_{50}$

In contrast, the $\text{Ti}_{25}\text{Al}_{75}$ alloy, which is composed of a TiAl_3 phase, produced ultrafine titanate nanowires but required 9 hours for the removal of Al. These results demonstrate that the TiAl_3 phase is necessary to produce the ultrafine nanowires and the existence of TiAl_3 nanocrystals enhances the Al leaching.



Scheme 2.4 Base treatment of $\text{Ti}_{25}\text{Al}_{75}$

The obtained nanowires are expected to possess remarkable ion-exchange properties because of their ultrafine diameters, which compose layered atomic structure and rough surfaces. In fact, the theoretical ion exchange capacity based on the composition of $\text{Na}_x\text{Ti}_{2-x/4}\text{O}_4$ ($x \doteq 1$) is $5.8 \text{ mequiv g}^{-1}$. The ICP-MS results show that the Sr^{2+} adsorption is proportional to the initial Sr^{2+} concentrations and is saturated at $3.8 \text{ mequiv g}^{-1}$ with the initial Sr^{2+} concentration of 2 mM (Fig. 2.17)

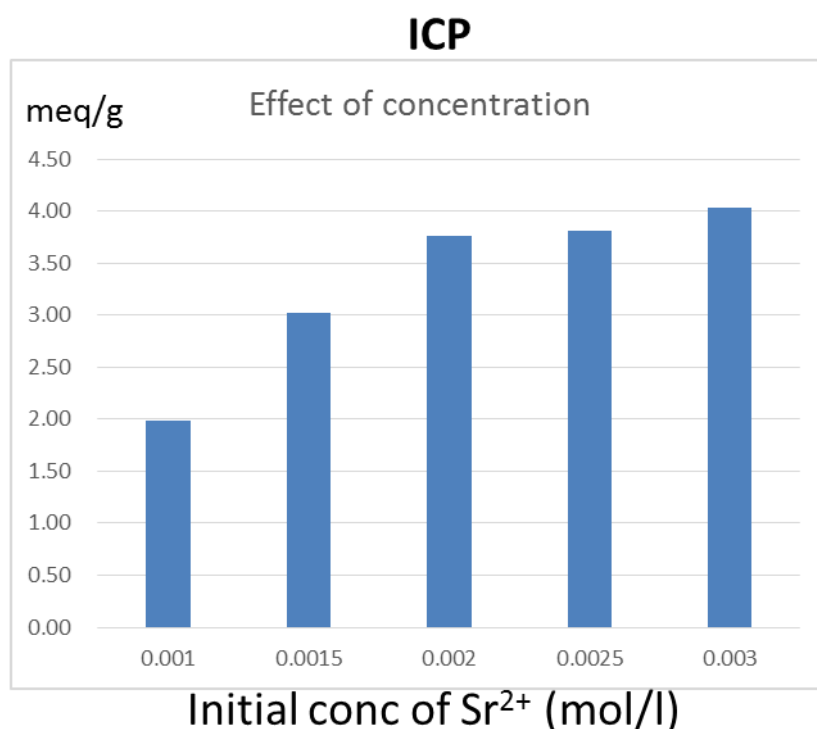


Figure 2.17 effect of concentration of initial Sr^{2+}
Amount of adsorbed Sr^{2+} calculated from ICP result

This result indicates that 66% of Na^+ is exchanged to Sr^{2+} . This value is outstanding because the previously reported experimental saturation capacities of related materials, $\text{Na}_2\text{Ti}_3\text{O}_7$ and $\text{Na}_{1.5}\text{Ti}_3\text{O}_7$ are only 19 and 22% of the theoretical capacity (1.26 and $1.14 \text{ mequiv g}^{-1}$), respectively.

In addition, Figure 2.26 shows that the uptake of Sr^{2+} speeds in an extremely fast event where the adsorption saturates within 5 min .

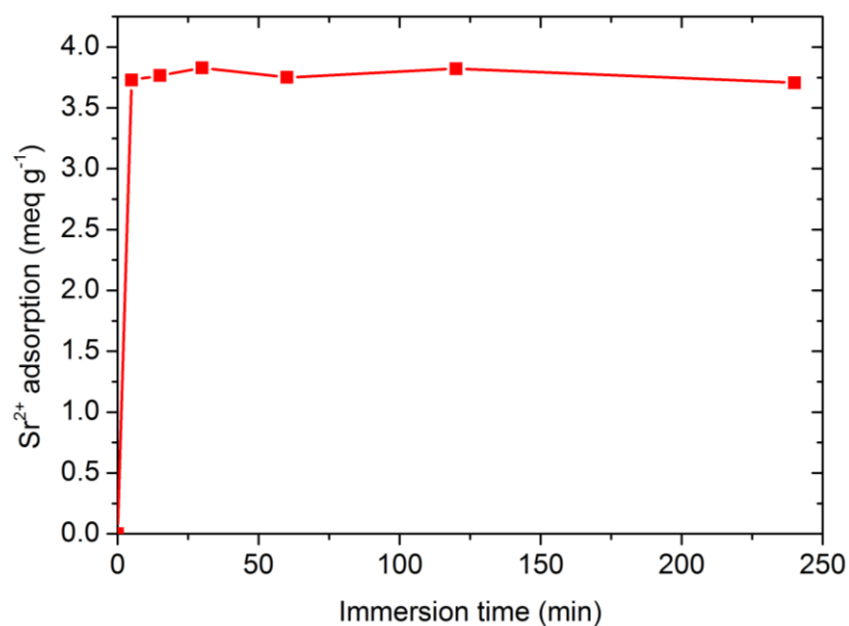


Figure 2.18 effect of treating time

The comparison with other reported materials is shown in Figure 2.19. A similar saturation capacity (3.56 mequiv g⁻¹) was reported with the K₄Nb₆O₁₇ nanolamina but the saturation required 300 min.

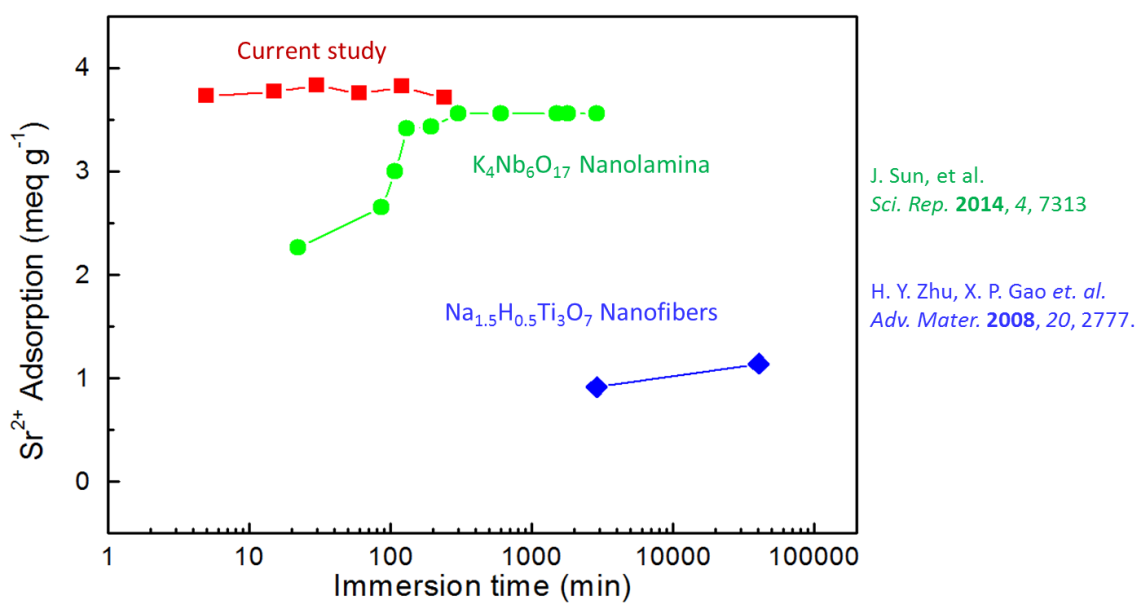


Figure 2.19 Comparison with reported materials

According to the Brunauer-Emmett-Teller (BET) measurements, a typical specific surface area is $369 \text{ m}^2 \text{ g}^{-1}$. In addition, the intercalated Na^+ cations can be exchanged with H^+ by neutralization with 0.1 M HCl aqueous solution, leading to hydrogen titanates. The BET specific surface area increased to $555 \text{ m}^2 \text{ g}^{-1}$ as a result of the expansion of the interlayer space, which was confirmed by the XRD results (Figure 2.20).

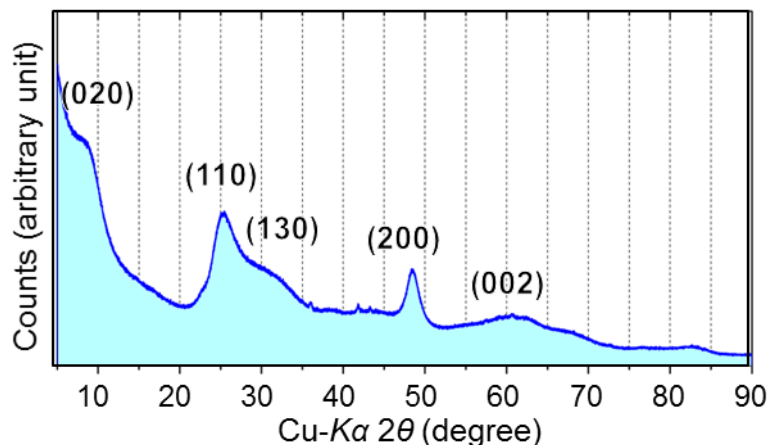


Figure 2.20 XRD of titanate nanowires after treated by HCl

With the $\text{Na}_2\text{Ti}_3\text{O}_7$ and $\text{Na}_{1.5}\text{H}_{0.5}\text{Ti}_3\text{O}_7$ nanofibers, the deformation was observed and the interlayer spaces were varied from 8.6 to 7.5 \AA and 7.5 to 7.1 \AA , respectively, after the Sr^{2+} adsorption. In contrast, the deformation of the present nanowires by Sr^{2+} adsorption is very small because the XRD measurements indicate that the variation of the interlayer space ranges from 9.1 to 9.0 \AA , which is negligible. Furthermore, the ultrafine nanowire has a much wider interlayer space. These facts suggest that the ion-exchange can be easily accomplished for the present nanowires.

The Barrett-Joyner-Halenda (BJH) pore size distribution plots based on N_2 adsorption isotherm experiments are shown in Figure 2.21. These result clearly show there is no signature of mesoporous and nanotube structures in the nanowires.

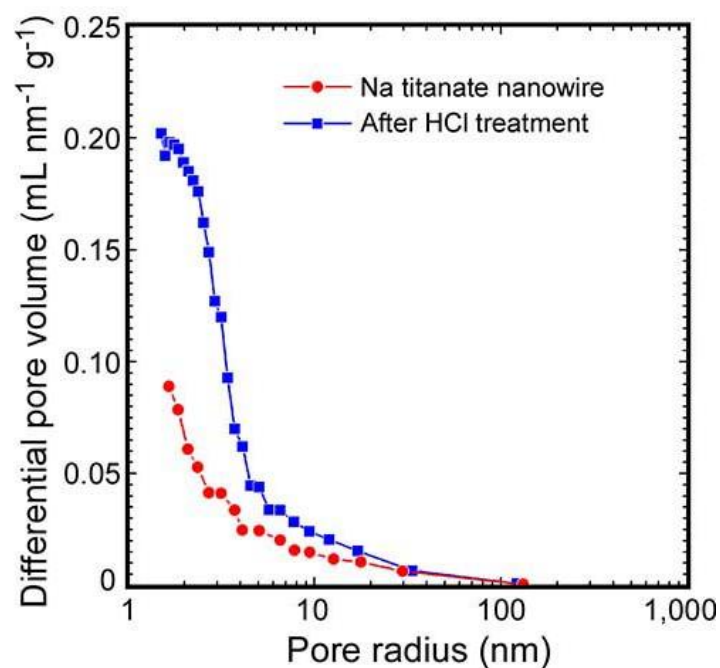


Figure 2.21 BJH plot of sodium titanate nanowires and titanate nanowires after treated by HCl

Before the Sr^{2+} adsorption, EDS map identified that the Na^+ sites are homogeneously distributed in the nanowires (Figure 2.22). After the Sr^{2+} adsorption, Sr^{2+} ions were distributed homogeneously (Figure 2.23).

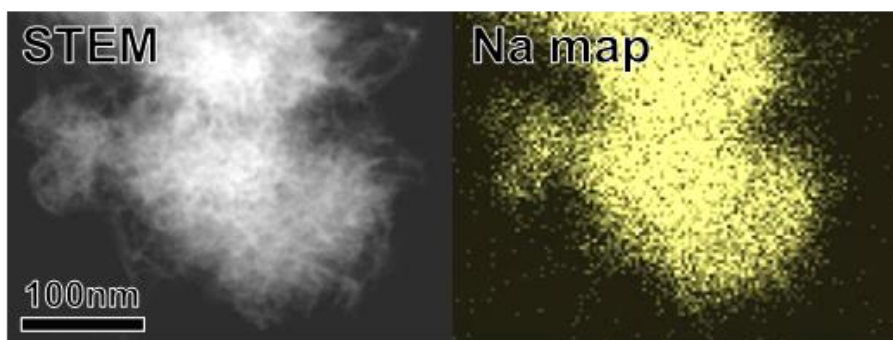


Figure 2.22 STEM image and Na mapping of sodium titanate nanowires

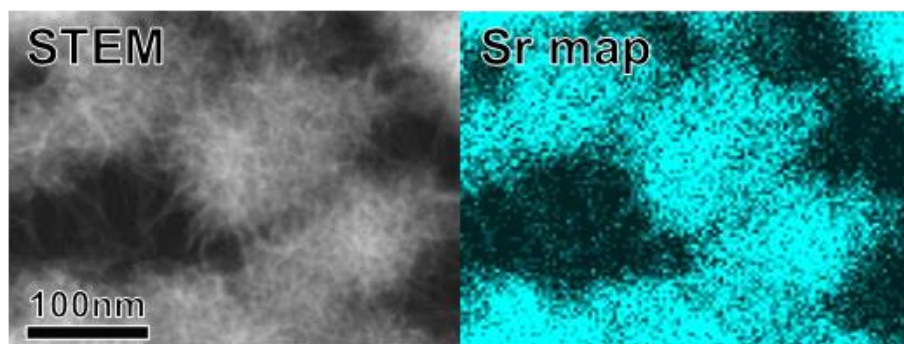


Figure 2.23 STEM image and Sr mapping of titanate nanowires after being used as Sr^{2+} ion exchanger

The EDS analysis of the adsorbed nanowires shows that the Na peak completely disappears and the Sr^{2+} was captured to nanowires (Figure 2.24).

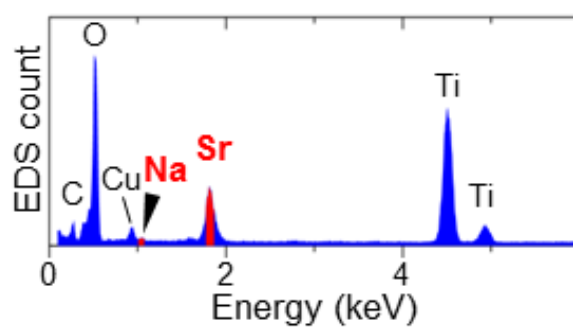


Figure 2.24 EDX of titanate nanowires after being used as Sr^{2+} ion exchanger

The pH effect shows that the near maximal adsorption is observed in the pH range of 4 - 11, whereas the adsorption ability becomes smaller at pH = 3 because of the partial ion-exchange of Na^+ with H^+ (Figure 2.25).

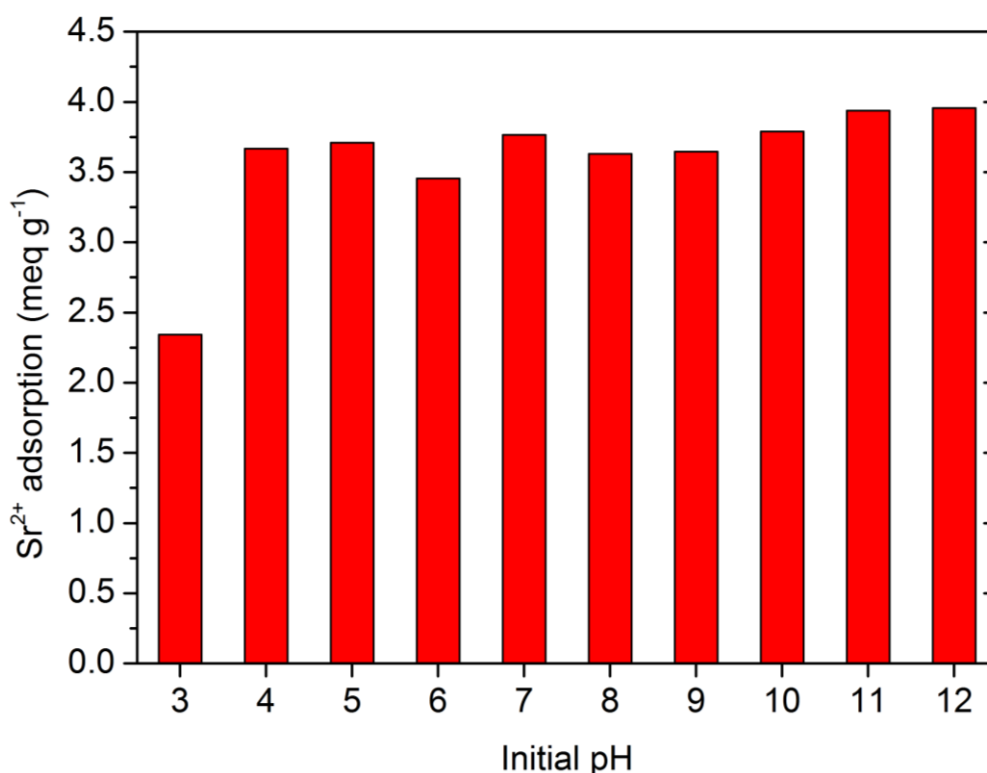


Figure 2.25 Dependence of pH on the Sr ion exchange in the nanowires

The present nanowires prefer to uptake Sr²⁺ over Na⁺ even with 50 times excess of sodium ions; thus Na⁺ ions was not detected by EDX analysis (Figure 2.26).

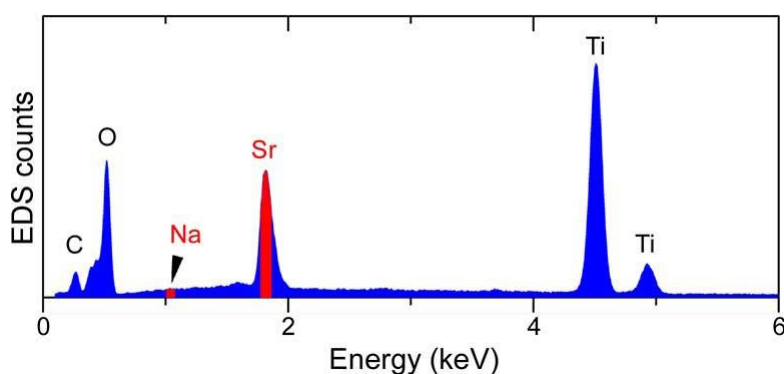


Figure 2.26 EDX of titanate nanowires after being used as Sr²⁺ ion exchanger with excess amount of Na⁺ ions

In addition, cation selectivity based on Gibbs exchange energies in zeolites has been reported that the exchange energy of Ba²⁺ is lower than that of Sr²⁺. We examine the Ba adsorption with the current nanowires, which is important because Ba²⁺ ions have a

similar ionic diameter as radioactive ^{226}Ra ions and show similar ion-exchange behavior.³⁸

The results shown in Figure 2.27 shows that the Ba^{2+} adsorption saturates at $4.3 \text{ mequiv g}^{-1}$ with an initial concentration of 2.5 mM . This result also demonstrate that Na ions were exchanged with Ba ions at 74% of the theoretical capacity.

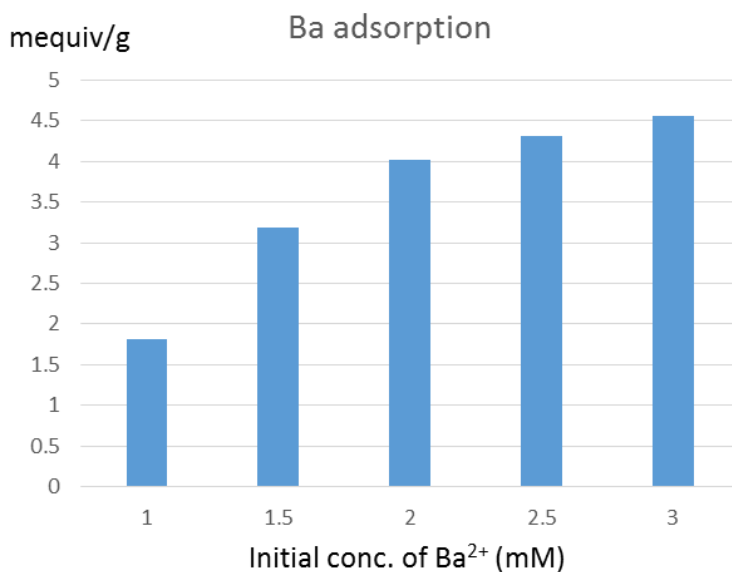


Figure 2.27 Effect of concentration of initial Ba^{2+}
Amount of adsorbed Ba^{2+} calculated from ICP results

In summary, we demonstrated a new method to create ultrafine sodium titanate nanowires and characterized their crystal structures. The key to creating such ultrafine nanowires is the simultaneous leaching and oxidizing of the rapidly solidified $\text{Ti}_6\text{Al}_{94}$ alloy, which includes TiAl_3 intermetallic compound nanocrystals. The nanowires are composed of unique atomic structures of layered TiO_6 -octahedra units and intercalated layers. These layered structures in the nanowires are important because they represent the extraordinary Sr ion exchange capacity as well as the extremely fast adsorption speed. These nanowires exhibit obvious potential application is not limited to adsorbents but also opens up new possibilities in battery electrodes, photo catalysts, and fiber reinforced materials.

3. Reference

1. P. C. Burns, R. C. Ewing, A. Navrotsky, A. *Science* **2012**, *335*, 1184.
2. K. O. Buesseler, *Science* **2012**, *338*, 480.
3. N. Yoshida, J. Kanda, *Science* **2012**, *336*, 1115.
4. D. Yang, H. Liu, Z. Zheng, S. Sarina, H. Zue, *Nanoscale* **2013**, *5*, 2232.
5. D. J. Yang, Z. F. Zheng, H. Y. Zhu, H. W. Liu, X. P. Gao, *Adv. Mater.* **2008**, *20*, 2777.
6. T. Kasuga, M. Hiramatsu, A. Hoson, T. Sekino, K. Niihara, *Langmuir* **1998**, *14*, 3160.
7. X. Wang, Z. Li, J. Shi, Y. Yu, *Chem. Rev.* **2014**, *114*, 9346.
8. H. Wang, Z. Guo, S. Wang, W. Liu, *Thin Solid Films* **2014**, *558*, 1.
9. Y. Xia, P. Yang, Y. Sun, Y. Wu, B. Mayers, B. Gates, Y. Yin, F. Kim, H. Yan, H. *Adv. Mater.* **2003**, *15*, 353.
10. X. Chen, S. S. Mao, *Chem. Rev.* **2007**, *107*, 2891.
11. Y. Komatsu, Y. Fujiki, T. Sasaki, *Anal. Sci.* **1991**, *7*(Supple), 153.
12. Database of Atomic Energy Society of Japan Home Page. <http://www.nuce-aesj.org/projects/clwt:start> (accessed March 5, **2015**).
13. W. J. Paulus, S. Komarneni, R. Roy, *Nature* **1992**, *357*, 571.
14. J. Sun, D. Yang, C. Sun, L. Liu, S. Yang, Y. Jia, R. Cai, X. Yan, *Sci. Rep.* **2014**, *4*, 7313.
15. D. V. Bavykin, J. M. Friedrich, F. C. Walsh, *Adv. Mater.* **2006**, *18*, 2807.
16. N. Li, L. Zhang, Y. Chen, M. Fang, J. Zhang, H. Wang, *Adv. Funct. Mater.* **2012**, *22*, 835.

17. Y. Li, X. Sun, *Chem. Eur. J.* **2003**, *9*, 2229.
18. Y. Mao, S. S. Wong, *J. Am. Chem. Soc.* **2006**, *128*, 8217.
19. A. -L. Sauvet, S. Baliteau, C. Lopez, P. J. Fabry, *Solid State Chem.* **2004**, *177*, 4508.

4. Experimental section

General information

Powder X-ray diffraction (XRD) measurements were performed by Rigaku SmartLab high-resolution X-ray diffractometer. The rotating anode generator with Cu K α radiation was used. The tube voltage and current was 45 kV and 200 mA, respectively. JEOL JSM-6500FE scanning electron microscopy (SEM) equipped with an energy dispersive X-ray spectroscopy (EDS; Oxford Instruments, X-Max 50) was used for the microstructure characterizations. The JEOL JEM-2010F scanning/transmission electron microscopy (S/TEM) with an accelerating voltage of 200 kV equipped with EDS (Oxford Instruments, X-Max 80) was used for the nanostructure characterizations. By making the electron beam size converge down to approximately 1 nm in diameter, nano-beam diffraction patterns (NBDPs) were obtained to identify the crystal structures and crystallographic orientations of the nanowires. High-resolution TEM (HRTEM) images were taken by a FEI TITAN80-300 aberration-corrected TEM operated at an accelerating voltage of 200 kV. The BET specific surface area of the prepared samples was obtained by using Quantachrome Quadrasorb. The ICP-MS measurements were performed with Agilent 8800.

Preparation of TiAl alloy ribbon

Highly-pure Ti (99.99%) and Al (99.99%) grain was melted with an electric arc-melting furnace in an Ar atmosphere. The atomic ratio of Ti : Al was 6 : 94. The alloy ribbons were prepared by the single-roller melt spinning that allow the rapid solidification of Ti₆Al₉₄ alloy and the homogeneous distribution of TiAl₃ intermetallic compound nanocrystals in Al matrix. The thickness of the ribbons is measured to be about 20 μ m.

Nanowire preparation

The Ti₆Al₉₄ ribbon (750 mg) was treated in 300 mL of 5 M NaOH aqueous solution for 4 hours at room temperature. Visually, white turbid liquid dispersed by fine powders was formed. The powders were separated by centrifugation at 10,000 rpm for 1 min, and washed with 50 mM NaOH three times, and then rinsed with acetone. Finally, NaTi_{1.75}O₄ nanowire were dried in vacuum and the visual appearance is to be white fine powders (146 mg). The overall yield is 94%.

Sr²⁺ and Ba²⁺ adsorption experiments

The aqueous solution of SrCl₂ or BaCl₂ (4 mL) with given concentrations was added to

the sodium titanate (4 mg) at room temperature at the desired pH, which was controlled by addition of 1 M HCl or 1 M NaOH. After the mixture was stirred for the required time, the adsorbent was separated by centrifugation at 10,000 rpm for 1 min, and washed with distilled water two times and acetone two times. The concentration measurement of the solution and the elemental analysis of the adsorbent were conducted with ICP-MS.

Chapter 3

Cerium oxide nanorods with unprecedented
low temperature oxygen storage capacity

1, Introduction

Shape and size controlled fabrication of inorganic nanomaterials is one of the ventral issues in nanotechnology because their chemical and physical properties are highly depends on their structures.¹ Particularly, 1D nanostructures, such as nanorods, nanowires, nanotubes, and nanobelts, have attracted great attention because of their unique electronic, optical, and mechanical properties and their applications in a variety of research fields, including catalysis, optoelectronics, and nanoelectronics.²

A number of fabrication methods have been reported, but most of them required high temperature conditions, which promote crystal growth with decrease of surface areas.³ In the chapter 2, I reported a new fabrication method of a Ti-Al alloy compound.⁴ The process involves the selective leaching of Al and the oxidation of Ti under nonthermal conditions, which allows the construction of metastable layered structure with remarkable Sr ion exchange ability.

Cerium oxide has been extensively studied owing to its high oxygen storage capacity (OSC), which is one of the most important features for the three-way catalysts (TWCs) for controlling exhaust emissions from automobile combustion engines.⁵ Particularly, the development of low temperature TWCs is strongly required for future fuel efficient vehicles for the protection of the environment.⁶ In this regard, considerable efforts have been made to design and synthesize a variety of cerium oxide nanomaterials.⁷ Nevertheless, the development of cerium oxide with effective OSC at low temperature is still a challenging issue.⁸ Recently, cerium oxide cubic nanocrystals have been reported to have low-temperature OSC properties, but need organic surfactants in fabrication process for controlling (100) facets under supercritical hydrothermal conditions.⁹ In this chapter, we report fine cerium oxide nanorods produced by simple corrosion method of Ce-Al alloy compounds in alkaline medium under mild conditions where emphasis is on the absence of surfactant and template. The obtained ultrafine nanorods have several nanometers in diameter and up to 50 nm in length. Surprisingly, they exhibits a remarkable OSC performance under low temperatures. The formation and homogeneous distribution of $\text{Ce}_3\text{Al}_{11}$ intermetallic nanocrystals in the Al matrix in the mother Ce-Al alloy ribbon is key for production of fine nanorods.

2, Result and discussion

The $\text{Ce}_6\text{Al}_{94}$ mother ingot was prepared by arc melting in an Ar atmosphere, and was liquid quenched by melt spinning with a single roller machine to form the corresponding ribbons (Figure 3.1).

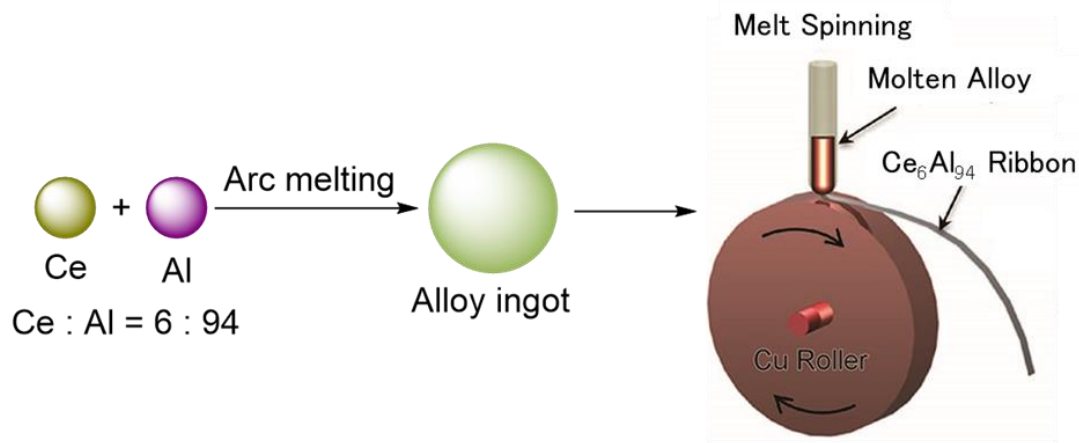


Figure 3.1 Fabrication scheme of $\text{Ce}_6\text{Al}_{94}$ alloy ribbon

The X-ray diffraction (XRD) profile of the ribbon indicates $\text{Ce}_3\text{Al}_{11}$ with the orthorhombic $\text{La}_3\text{Al}_{11}$ structure¹⁰ in addition to fcc Al¹¹ matrix (Figure 3.2).¹²

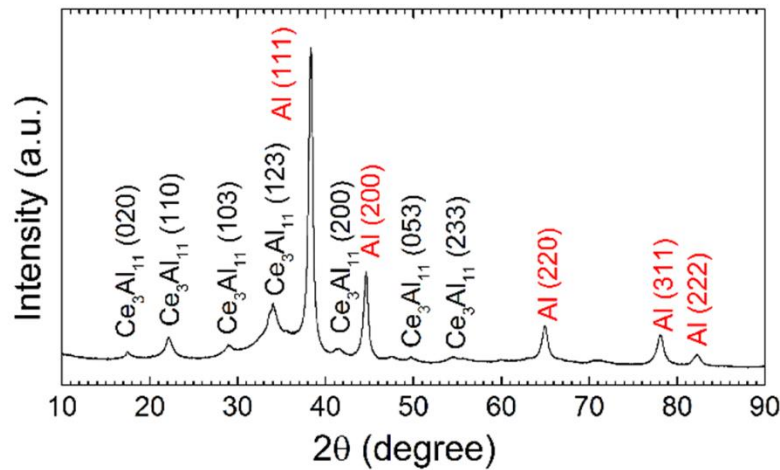


Figure 3.2 XRD profile of $\text{Ce}_6\text{Al}_{94}$ alloy ribbon

A bright field magnified transmission electron microscopy (TEM) observation for the ribbon shows that the $\text{Ce}_3\text{Al}_{11}$ nanocrystals with sizes of 5-30 nm in range are homogeneously distributed in the Al matrix (Figure 3.3). The inset of figure 3.3 shows

that the selected area electron diffraction (SAED) pattern confirms the phase separation of $\text{Ce}_3\text{Al}_{11}$ and Al, which is in excellent agreement with the XRD result.¹³

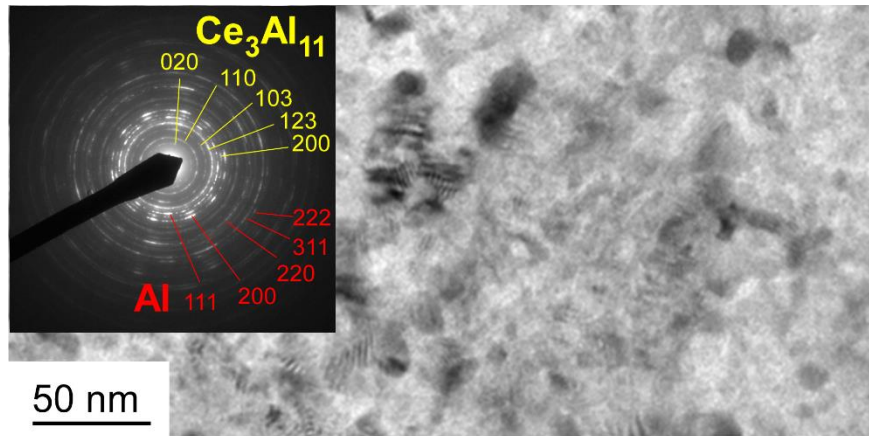


Figure 3.3 Bright field TEM image and NBEDP of $\text{Ce}_6\text{Al}_{94}$ alloy ribbon

Figure 3.4 shows a dark field magnified TEM image obtained at the diffracted 020 beam of $\text{Ce}_3\text{Al}_{11}$ nanocrystals. This image clearly shows the well dispersed $\text{Ce}_3\text{Al}_{11}$ structure of the size of 10 - 20 nm.

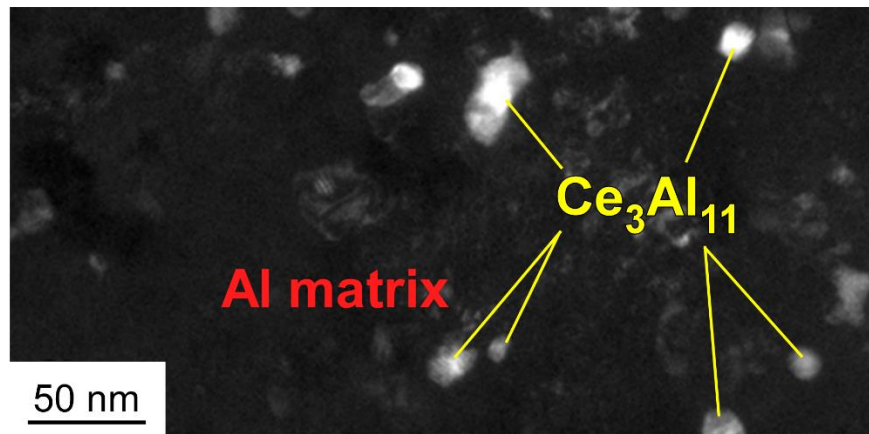
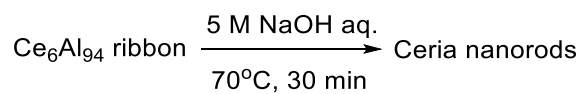


Figure 3.4 Dark field TEM image obtained at 020 beam $\text{Ce}_3\text{Al}_{11}$ of $\text{Ce}_6\text{Al}_{94}$ alloy ribbon

Treatment of the $\text{Ce}_6\text{Al}_{94}$ ribbons with 5 M NaOH aqueous solution at 70 °C results in the formation of precipitates with the evolution of hydrogen gas. The collected materials are washed with distilled water and acetone several times. After vacuum drying, the pale yellow powder was obtained (Figure 3.5) and the XRD profile shows that the peaks are assigned to CeO_2 (Figure 3.6).¹⁴



Scheme 3.1 Fabrication of ceria nanorods

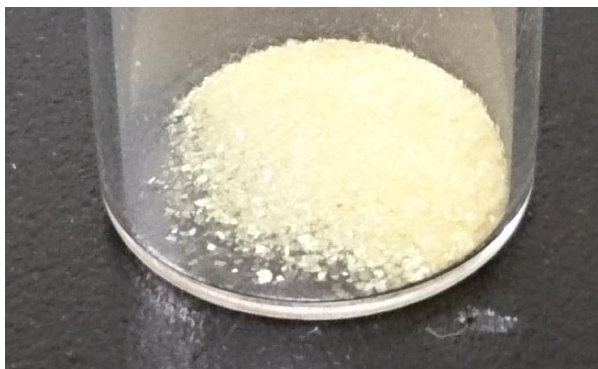


Figure 3.5 Picture of ceria nanorods obtained by dealloying method

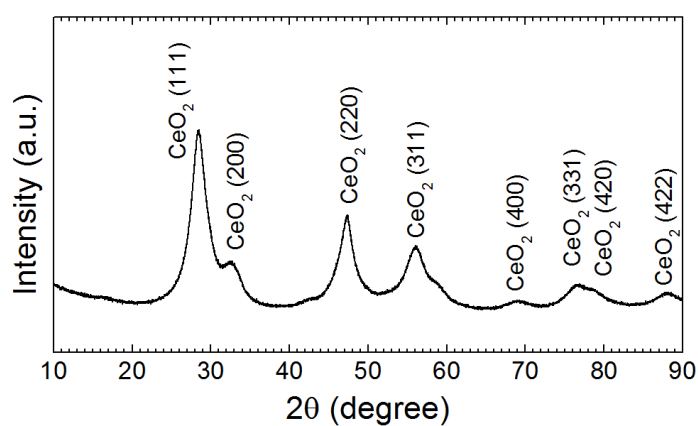


Figure 3.6 XRD profile of ceria nanorods

The bright-field TEM image of the obtained CeO_2 reveals the highly dense nanorods structures with a length up to 50 nm (Figure 3.7). The result of the SAED patterns (the inset of figure 3.7) confirms that the sample has a fluorite structure of CeO_2 , which is consistent with the XRD result.

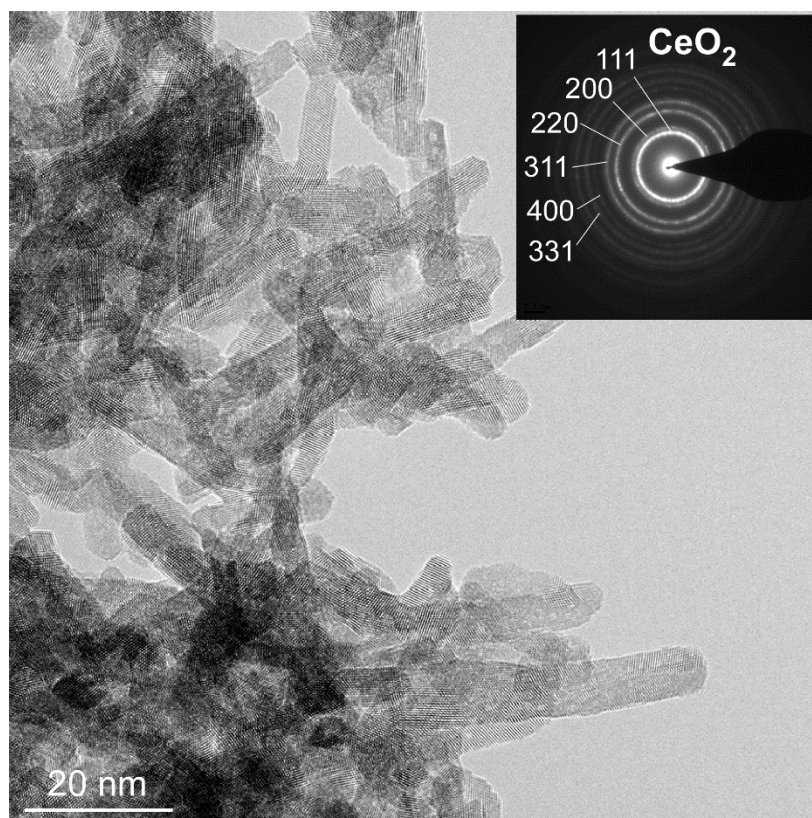


Figure 3.7 Bright field TEM image and NBDP of ceria nanorods

The energy dispersive X-ray spectroscopy (EDX) analysis shows that Al was dissolved nearly quantitatively (Figure 3.8). From the ICP-MS analysis, amount of Al in obtained nanowires was lower than 0.5 wt%.

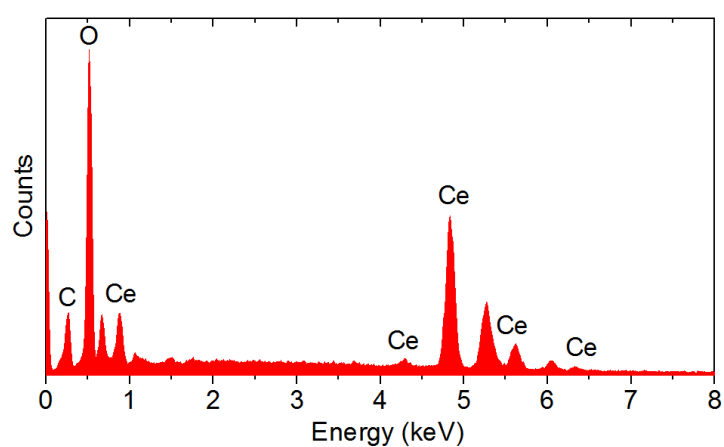


Figure 3.8 EDX spectra of ceria nanorods

Figure 3.9 shows a high-resolution (HR) TEM image of CeO_2 nanorods, revealing that the ultrafine diameter is approximately 5-7 nm and the crystallographic growth direction is mainly $\{011\}$. Furthermore, it demonstrates that the sidewall structures are composed of (100) surfaces. In contrast to a flat (111) surface, the (100) surface of the nanorods have significant roughness and such atomic structure can be recognized in this figure.

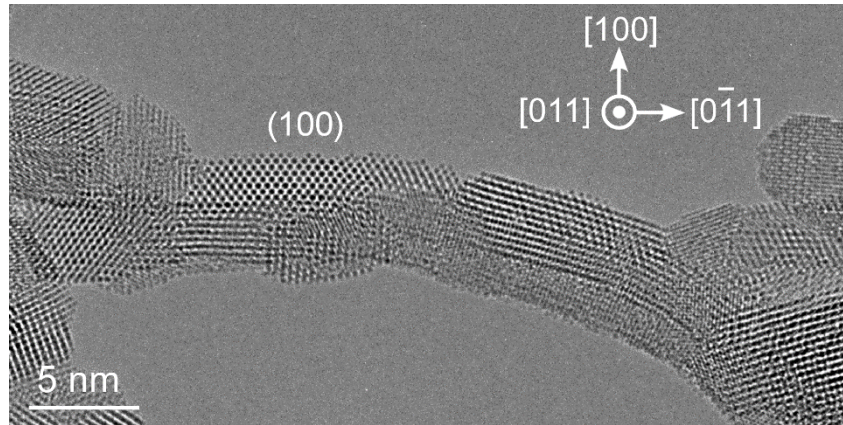


Figure 3.9 HRTEM image of ceria nanorods

According to the Brunauer-Emmett-Teller (BET) measurement, a typical specific surface area is $218 \text{ m}^2/\text{g}$.

Alternatively, the alloy thin films with thickness of $40 \text{ }\mu\text{m}$ are prepared from the $\text{Ce}_6\text{Al}_{94}$ alloy ingot by cold rolling instead of the melt spinning method.

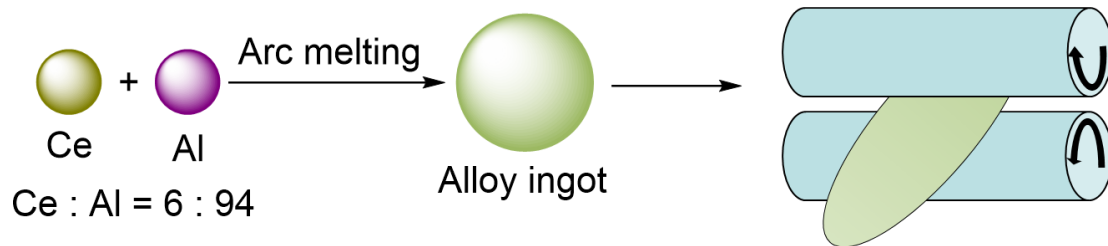


Figure 3.10 Fabrication scheme of $\text{Ce}_6\text{Al}_{94}$ alloy film

The XRD patterns shows that these films have also $\text{Ce}_3\text{Al}_{11}$ crystalline phase (Figure 3.11). However, the scanning electron microscopy (SEM) with EDX elemental mapping analysis indicate that crystal of $\text{Ce}_3\text{Al}_{11}$ is micrometer size (Figure 3.12), which is much larger than that in the alloy ribbon.

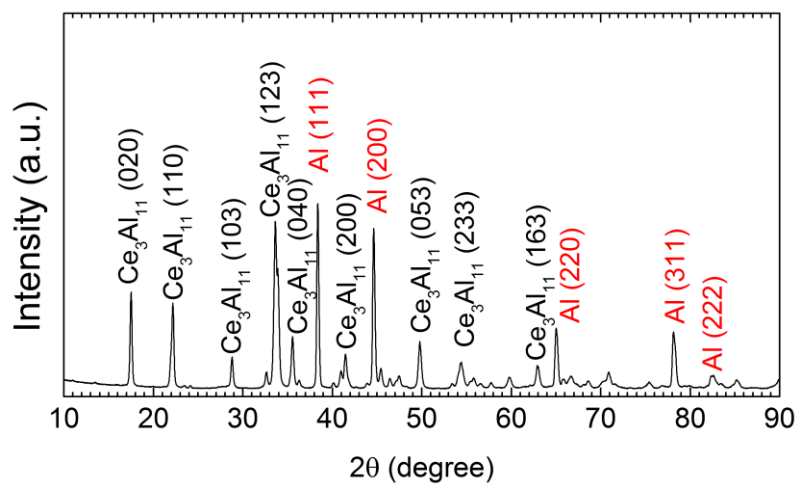


Figure 3.11 XRD profile of $\text{Ce}_6\text{Al}_{94}$ alloy film

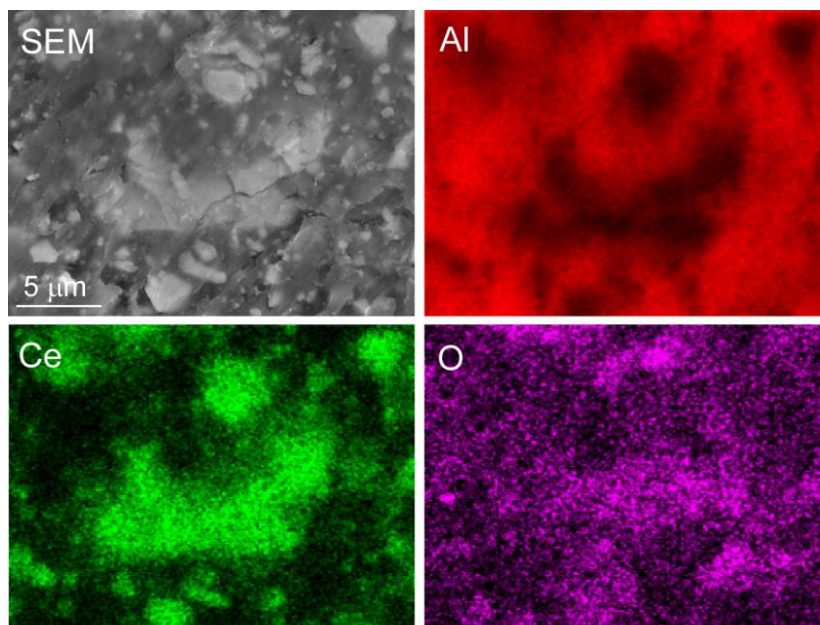
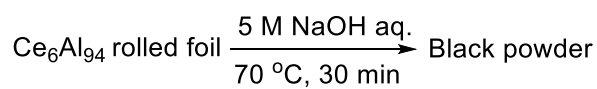


Figure 3.12 SEM image and EDX mapping of $\text{Ce}_6\text{Al}_{94}$ alloy film

Interestingly, when the Ce-Al alloy thin film were dealloyed under the same conditions, the nanorods were formed only on the film surfaces, and Al remained without dissolution.



Scheme 3.2 Base treatment of alloy foil



Figure 3.13 Picture of base treated $\text{Ce}_6\text{Al}_{94}$ alloy film

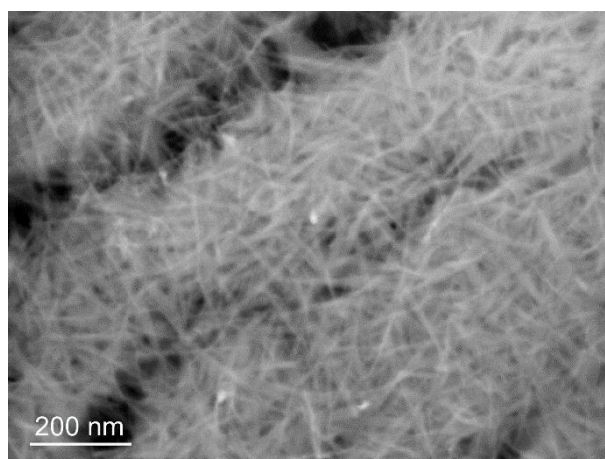


Figure 3.14 SEM image of base treated $\text{Ce}_6\text{Al}_{94}$ alloy film

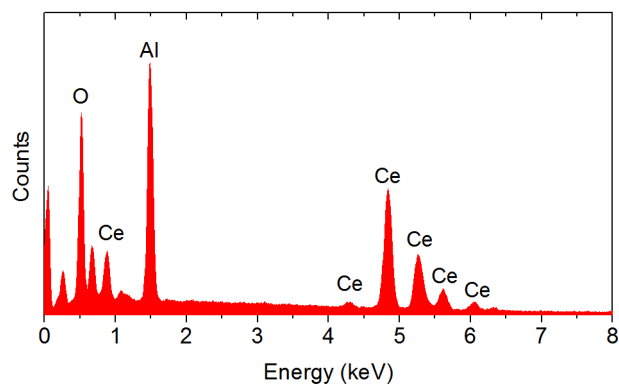
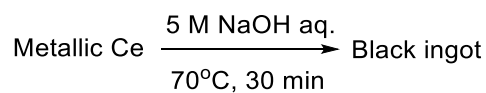


Figure 3.15 EDX spectra of base treated $\text{Ce}_6\text{Al}_{94}$ alloy film

Furthermore, the treatment of cerium metal grains with alkaline medium under the same conditions, did not give any nanorods structures (Figure 3.16).



Scheme 3.3 Base treatment of metallic Ce

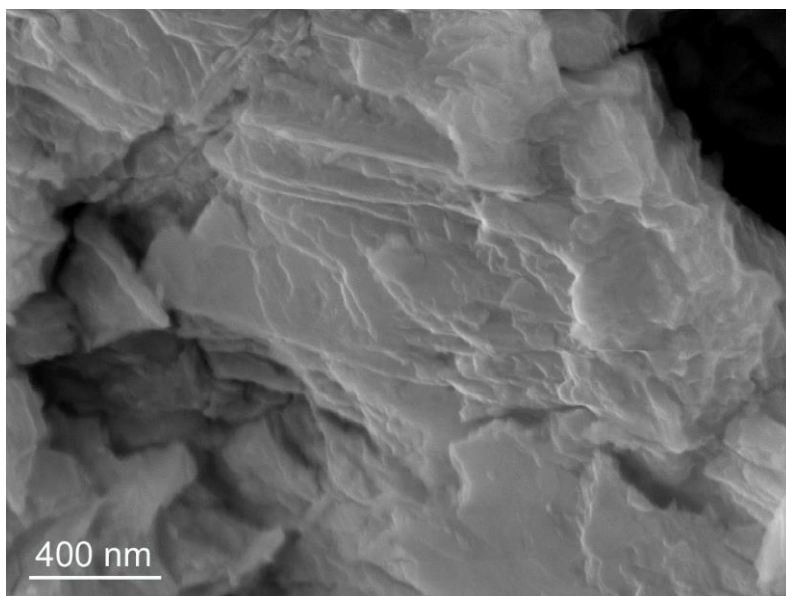


Figure 3.16 SEM image of base treated metallic Ce

These result clearly indicate that the formation and homogeneous distribution of $\text{Ce}_3\text{Al}_{11}$ nanocrystals in the Al matrix by the rapid quenching with the melt spinning system is key to the fabrication of ultrafine nanorods.

The OSC measurement of the present cerium oxide nanorods were conducted by use of thermogravimetric analysis (TGA). As a pretreatment the sample was heated to 200 °C and kept for 6 h under N₂ flow conditions to stabilize the baseline (Figure 3.17) Then, 2% H₂/N₂ and 2% O₂/N₂ were alternately introduced at various temperatures, and the resulting mass change was converted to OSC (Figure 3.18-3.20).

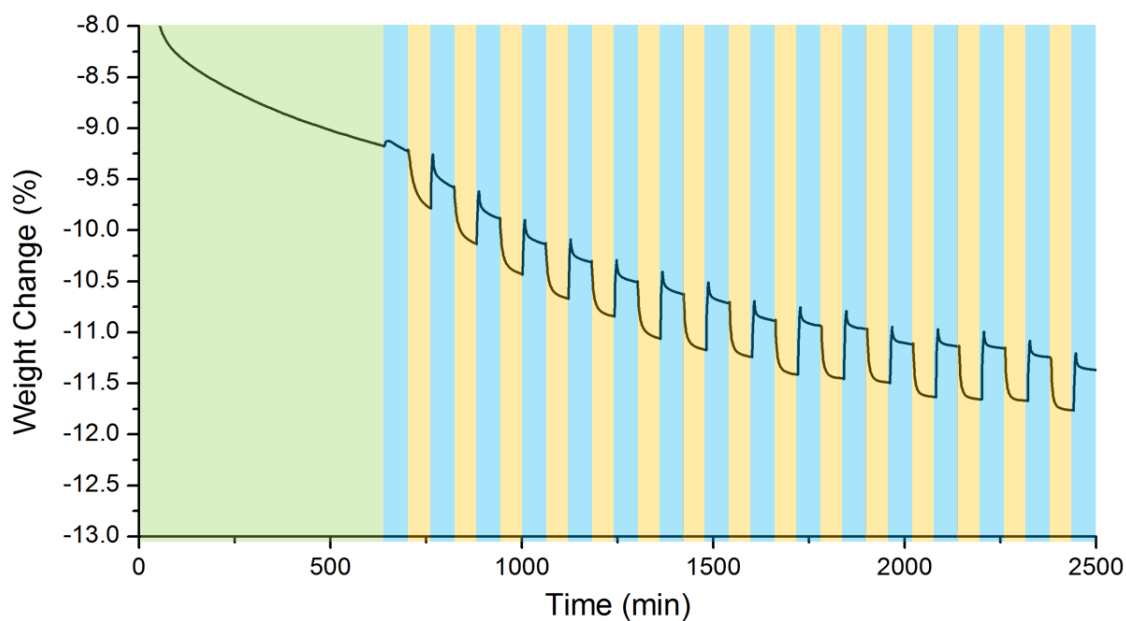


Figure 3.17 Initial TGA result at 200 °C

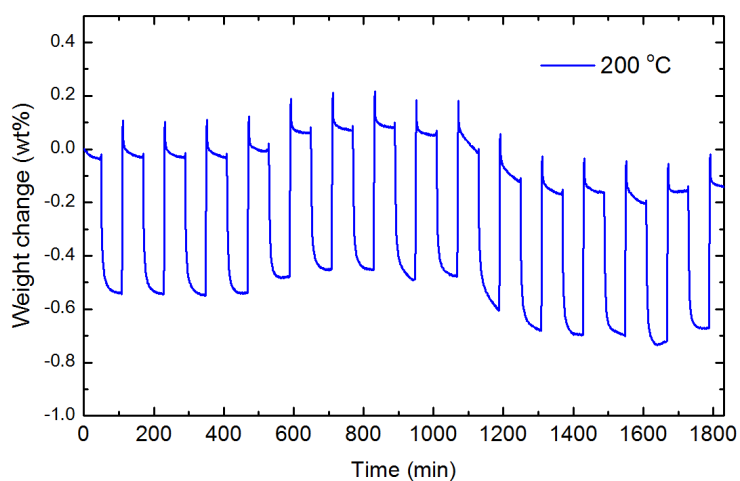


Figure 3.18 Stabilized TGA result at 200 °C

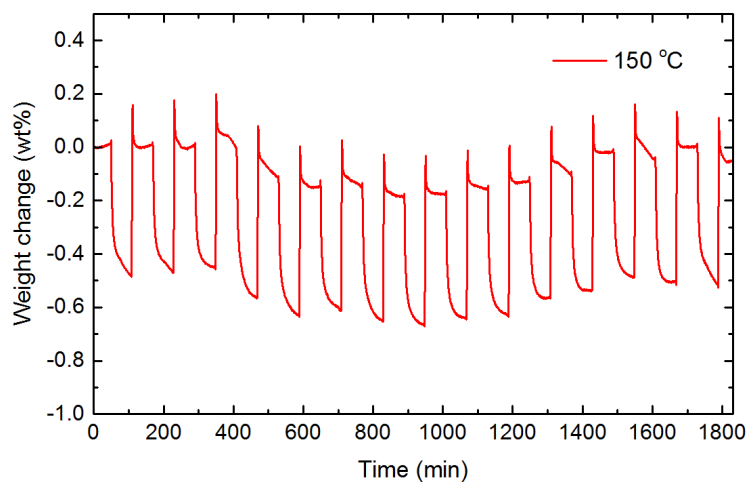


Figure 3.19 Stabilized TGA result at 150 °C

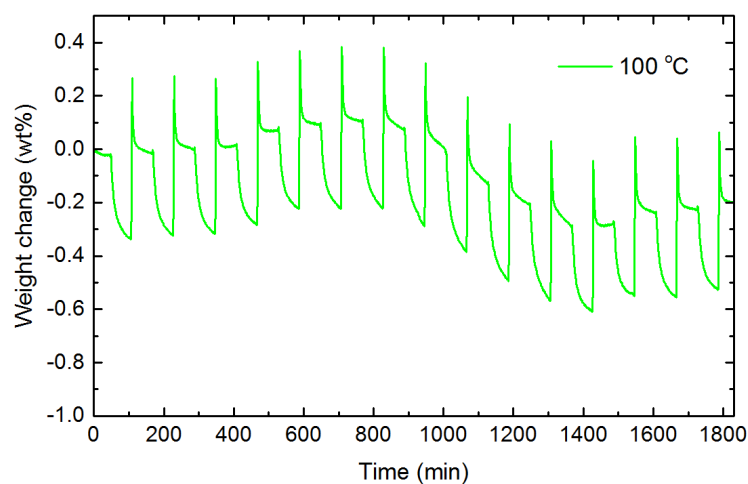


Figure 3.20 Stabilized TGA result at 100 °C

We started the OSC measurement at 200 °C. When the H_2/N_2 gas was induced, weight of nanorods decreased by the releasing of oxygen and finally weight loss was leached to 0.5% which corresponds to the OSC of 156 $\mu\text{mol O}_2/\text{g}$. Then, by changing the gas from hydrogen to oxygen, nanorods were quickly oxidized under the oxidative conditions and the weight was gone back to the original weight.

The result is outstanding because the reported nanocubes with (100) facets exhibit less than 35 $\mu\text{mol O}_2/\text{g}$ at the same temperature. These results encouraged me to examine the OSC at lower temperature. The nanorods showed the OSC at 150 °C with 140 μmol

O₂/g, which is five times more than that of the nanocubes. Furthermore, the OSC was observed even at 100 °C with 81 μmol O₂/g (Figure 3.21).

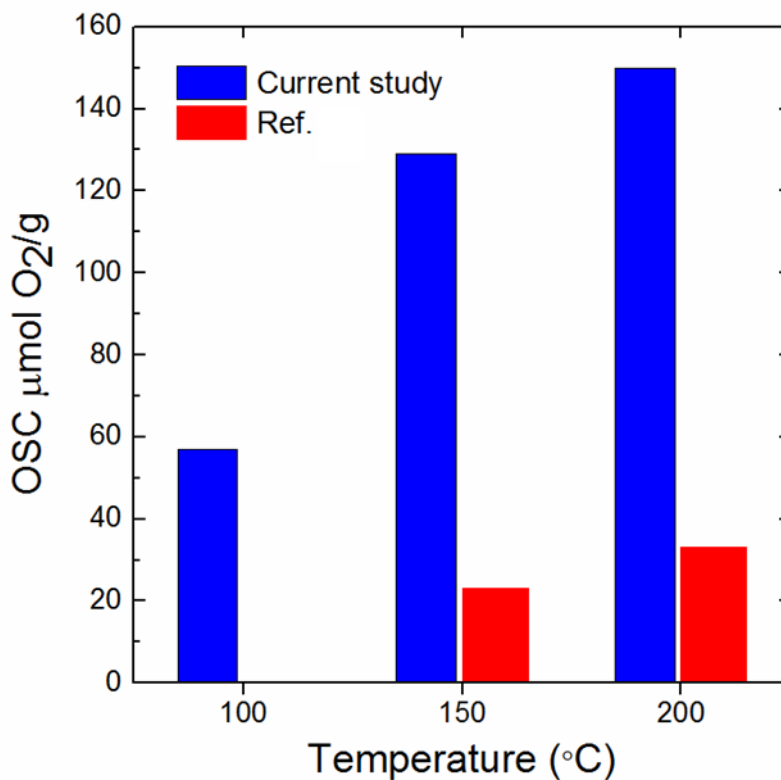


Figure 3.21 Summarized TGA results

Previous theoretical studies on CeO₂ suggest that the surface reactivity is higher on the (100) surface than on either (110) or (111), and the exposure of more active (100) surfaces followed by (110) surfaces, should facilitate the formation of oxygen vacancies, and enhance the OSC.¹⁵ This is confirmed by HRTEM obtained after the OSC measurements, as shown in Figure 3.22. Significantly rough surface on (100) can be recognized. The improved crystallinity is observed by XRD (Figure 3.23).

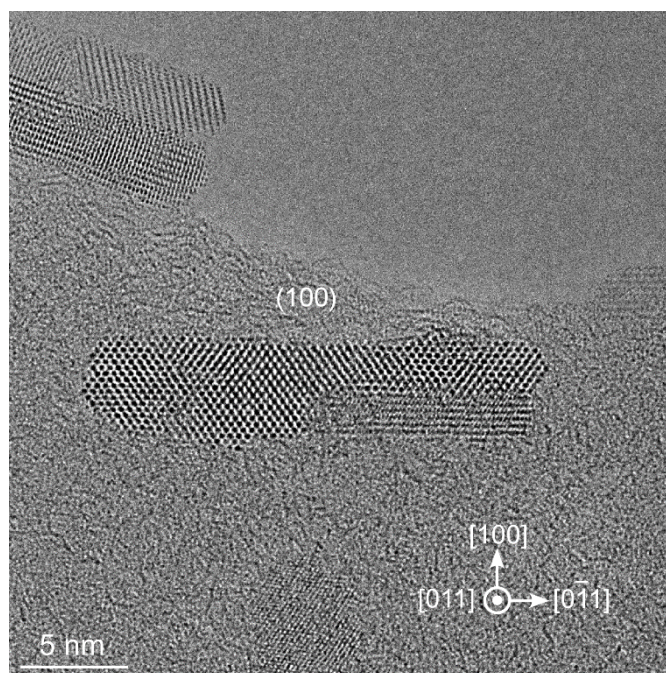


Figure 3.22 HRTEM image of ceria nanorods after being used at 200 °C

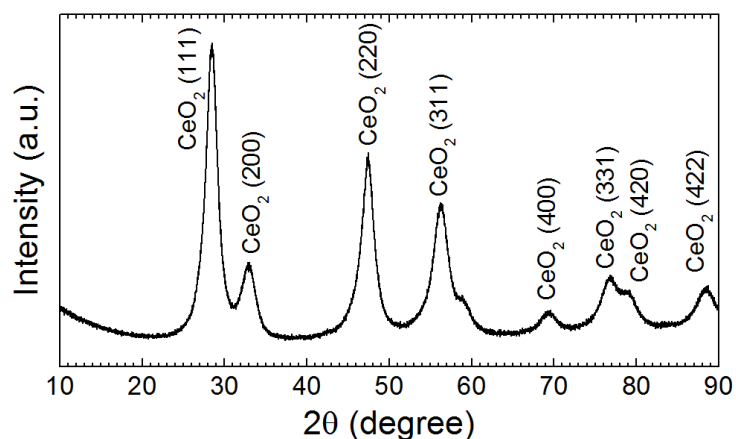


Figure 3.23 XRD profile of ceria nanorods after being used at 200 °C

The observed high performance at low temperature would be ascribed to the reactive surface on the current nanorods. It is known that surface few layers of CeO₂ contribute to OSC, therefore, CeO₂ with large specific surface area has advantage for OSC. The BET surface area is 194 m²/g after the OSC measurement at 200 °C.

The OSC value per surface area of CeO₂ nanorods ($156 \mu\text{mol O}_2 \text{ g}^{-1} / 194 \text{ m}^2 \text{ g}^{-1} = 0.80 \mu\text{mol O}_2 \text{ m}^{-2}$) is higher than that of the cubic (100) CeO₂ in reference 9c ($35 \mu\text{mol O}_2 \text{ g}^{-1} /$

$61 \text{ m}^2 \text{ g}^{-1} = 0.57 \text{ } \mu\text{mol O}_2 \text{ m}^{-2}$) at $200 \text{ }^\circ\text{C}$.^{9c} These results clearly show that the observed high OSC is not only due to the large surface area but also due to the nanorods surface structures.

In summary, I have demonstrated a new fabrication method of fine cerium oxide nanorods by the simple corrosion method. The process proceeds through the leaching of Al and the oxidation of Ce in the rapidly solidified $\text{Ce}_6\text{Al}_{94}$ alloy under mild conditions. The key to create such ultrafine nanorods is the formation and homogeneous distribution of $\text{Ce}_3\text{Al}_{11}$ intermetallic compound nanocrystals in the Al matrix in the mother alloy ribbons. They represent the excellent low temperature OSC performance compared to the previously reported cerium oxide nanomaterials. These nanorods exhibit obvious potential applications as the three way catalyst. Furthermore, their application is not limited to OSC materials but also opens up new possibilities in catalysis, fuel cells, UV blockers, solar cells, and sensors.

3. Reference

1. a) Y. Li, W. J. Shen, *Sci. China Chem.* **2012**, *55*, 2485.
b) T.-D. Nguyen, *Nanoscale* **2013**, *5*, 9455.
c) Y. Li , W. Shen , *Chem. Soc. Rev.* **2014** , *43* ,1543.
2. a) Kenry, C. T. Lim, *Prog. Mater. Sci.* **2013**, *58*, 705.
b) B. Weng, S. Liu, Z.-R. Tang, Y.-J. Xu, *RSC Adv.* **2014**, *4*, 12685.
c) H. Sun, J. Deng, L. Qiu, X. Fang, H. Peng, *Energy Environ. Sci.* **2015**, *8*, 1139.
d) W. Tian, H. Lu, L. Li, *Nano Res.* **2015**, *8*, 382.
e) F.-X. Xiao, J. Miao, H. B. Tao, S.-F. Hung, H.-Y. Wang, H. B. Yang, J. Chen, R. Chen, B. Liu, *Small* **2015**, *11*, 2115.
3. a) Y. Xia, P. Yang, Y. Sun, Y. Wu, B. Mayers, B. Gates, Y. Yin, F. Kim, H. Yan, *Adv. Mater.* **2003**, *15*, 353.
b) R. S. Devan, R. A. Patil, J.-H. Lin, Y.-R. Ma, *Adv. Funct. Mater.* **2012**, *22*, 3326.
c) M.-A. Einarsrud, T. Grande, *Chem. Soc. Rev.* **2014**, *43*, 2187.
4. Y. Ishikawa, S. Tsukimoto, K. S. Nakayama, N. Asao, *Nano Lett.* **2015**, *15*, 2980.
5. a) S. Matsumoto, *Catal. Today* **2004**, *90*, 183.
b) J. Kašpar, P. Fornasiero, N. Hockey, *Catal. Today* **2003**, *77*, 419.
c) M. Sugiura, M. Ozawa, A. Suda, T. Suzuki, T. Kanazawa, *Bull. Chem. Soc. Jpn.* **2005**, *78*, 752.
6. H.-Y. Chen, H.-L. Chang, *J. M. Technol. Rev.* **2015**, *59*, 64.
7. a) Q. Yuan, H.-H. Duan, L.-L. Li, L.-D. Sun, Y.-W. Zhang, C.-H. Yan, *J. Colloid Interface Sci.* **2009**, *335*, 151.
b) A. Bumajdad, J. Eastoe, A. Mathew, *Adv. Colloid Interface Sci.* **2009**, *56*, 147.
c) C. W. Sun, H. Li, L. Q. Chen, *Energy Environ. Sci.* **2012**, *5*, 8475.
d) D. Zhang, X. Du, L. Shi, R. Gao, *Dalton Trans.* **2012**, *41*, 14455.
e) N. Ta, J. Liu, W. Shen, *Chin. J. Catal.* **2013**, *34*, 838.
f) Z. A. Qiao, Z. Wu, S. Dai, *ChemSusChem* **2013**, *6*, 1821.
g) W. Huang, Y. Gao, *Catal. Sci. Technol.* **2014**, *4*, 3772.

8. a) H.-X. Mai, L.-D. Sun, Y.-W. Zhang, R. Si, W. Feng, H.-P. Zhang, H.-C. Liu, C.-H. Yan, *J. Phys. Chem. B* **2005**, *109*, 24380.
b) T. Yu, J. Joo, Y. I. Park, T. Hyeon, *Angew. Chem. Int. Ed.* **2005**, *44*, 7411.
c) Tana, M. Zhang, J. Li, H. Li, Y. Li, W. Shen, *Catal. Today* **2009**, *148*, 179.
d) L. González-Rovira, J. M. Sánchez-Amaya, M. López-Haro, E. del Rio, A. B. Hungria, P. Midgley, J. J. Calvino, S. Bernal, F. J. Botana, *Nano Lett.* **2009**, *9*, 1395.
e) D. Wang, Y. Kang, V. Doan-Nguyen, J. Chen, R. Küngas, N. L. Wieder, K. Bakhmutsky, R. J. Gorte, C. B. Murray, *Angew. Chem. Int. Ed.* **2011**, *50*, 4378.
f) C. Sun, D. Xue, *Phys. Chem. Chem. Phys.* **2013**, *15*, 14414.
g) J. Li, Z. Zhang, Z. Tian, X. Zhou, Z. Zheng, Y. Ma, Y. Qu, *Mater. Chem. A* **2014**, *2*, 16459.
h) X. -F. Yu, J. -W. Liu, H. -P. Cong, L. Xue, M. N. Arshad, H. A. Albar, T. R. Sobahi, Q. Gao, S. H. Yu, *Chem. Sci.* **2015**, *6*, 2511.

9. a) J. Zhang, S. Ohara, M. Umetsu, T. Naka, Y. Hatakeyama, T. Adschiri, *Adv. Mater.* **2007**, *19*, 203.
b) K. Kaneko, K. Inoke, B. Freitag, A. B. Hungria, P. A. Midgley, T. W. Hansen, J. Zhang, S. Ohara, T. Adschiri, *Nano Lett.* **2007**, *7*, 421.
c) J. Zhang, H. Kumagai, K. Yamamura, S. Ohara, S. Takami, A. Morikawa, H. Shinjoh, K. Kaneko, T. Adschiri, A. Suda, *Nano Lett.* **2011**, *11*, 361.

10. J. X. Boucherle, F. Givord, G. Lapertot, A. Muñoz, J. Schweizer, *J. Magn. Magn. Mater.* **1995**, *148*, 397.

11. S. Popovic', B. Gržeta, V. Ilakovac, R. Kroggel, G. Wendrock, H. Löffler, *Phys. Status Solidi A* **1992**, *130*, 273.

12. G. Borzone, G. Cacciamani, R. Ferro, *Metall. Mater. Trans. A* **1991**, *22*, 2119.

13. K. A. Gschneidner Jr., F. W. Calderwood, *Binary Alloy Phase Diagrams, Vol. 1*, (Ed: T. B. Massalski), ASM International, **1990**.

14. J. R. McBride, K. C. Hass, B. D. Poindexter, W. H. Weber, *J. Appl. Phys.* **1994**, *76*, 2435.

- 15 a) T. X. T. Sayle, S. C. Parker, C. R. A. Catlow, *Surf. Sci.* **1994**, *316*, 329.

b) J. C. Conesa, *Surf. Sci.* **1995**, *339*, 337.

c) D. C. Sayle, S. A. Maicaneanu, C. A. Watson, *J. Am. Chem. Soc.* **2002**, *124*, 11429.

4. Experimental section

General information

Powder XRD measurements were performed by Rigaku SmartLab high-resolution X-ray diffractometer. The rotating anode generator with Cu K α radiation was used. The tube voltage and current were 45 kV and 200 mA, respectively. JEOL JSM-6500FE SEM equipped with energy-dispersive X-ray spectroscopy (EDS) (Oxford Instruments, X-Max 50) was used for the microstructure characterizations. The JEOL JEM-2010F scanning/transmission electron microscopy (S/TEM) with an accelerating voltage of 200 kV equipped with EDS (Oxford Instruments, X-Max 80) was used for the nanostructure characterizations. SAED patterns were obtained to identify the crystal structures of the Ce–Al alloys and CeO₂ nanorods. HRTEM images were taken by a FEI TITAN80-300 aberrationcorrected TEM operated at an accelerating voltage of 200 kV. The BET specific surface area of the prepared samples was obtained by using Quantachrome Quadrasorb. The OSC measurements are carried out on Rigaku thermo plus EVO II / TG8120.

Preparation of Ce–Al Alloy Ribbon

Highly pure Ce (99.9%) with the grain sizes of 2–3 mm and highly pure Al (99.99%) with the grain sizes of 5–8 mm were melted in an electric arc-melting furnace (Divac Limited, ACM-S01 TMP) in a 0.05 MPa Ar atmosphere. The arc current was about 200 A. The atomic ratio of Ce:Al was 6:94. The alloy ribbons were prepared by the single-roller melt spinning (3400 rpm) that allow the rapid solidification of Ce₆Al₉₄ alloy and the homogeneous distribution of Ce₃Al₁₁ intermetallic compound nanocrystals in Al matrix. The thickness of the ribbons is measured to be about 20 μ m.

Nanorods Preparation

The Ce₆Al₉₄ ribbon was treated in 5 M NaOH aqueous solution for 15 min at 70 °C. After decantation of the mixture, the remained materials were treated again with 5 M NaOH repeatedly for 15 min at 70 °C. The resulting powders were separated by decantation, and washed with distilled H₂O more than five times, and then rinsed with acetone. Finally, the materials were dried in vacuum to give CeO₂ nanorods.

Preparation of Ce–Al Thin Film

About 7 g of Ce₆Al₉₄ alloy ingot was sandwiched between stainless steel boards and extended with cold rolling. The thickness of a thin film was 40 μ m.

Acknowledgement

This doctoral dissertation has carried out under the direction of Professor Naoki Asao at the Department of Chemistry, Graduate School of Science, Tohoku University, Japan.

I would like to express my sincerely gratitude to Professor Naoki Asao for his valuable comments, suggestions, and deep questions for my work. Thank you to teach me not only knowledge but also attitude for mu research.

I would also like to thank Professor Yoshinori Yamamoto for his supports and suggestions.

I am deeply grateful to Associate Professor Tienan Jin for his valuable discussion and technical advice, and also to Dr. Menggenbateer and Dr. Shinya Tanaka for their assistance not only with my work but also with my life.

I would like to appreciate Professor Koji Nakayama and Dr. Susumu Tsukimoto for collaboration, discussions, and suggestions in this study.

I am also thankful to Mr. Maiki Takeda, Ms. Man Zhang, Mr. Kento Ogata, Mr. Yuta Suzuki, Mr. Norihito Shiraiwa, Mr. Qilin Shi and every member of Asao's group for their kindness and constructive discussion.

I would like to express my acknowledgement to Dr. Ryotaro Kumashiro, Mr. Kesami Saito, Dr. Shin-ichi Yamaura, Mr. Katuhiro Abe, Mr. Kosei Kobayashi and Ms. Yoko Nakano for their support with the synthesis and characterization of my materials.

I would like to thank Japan Society for the Promotion of Science Fellowship for a grant that made it possible to complete this work.

Finally, I would like to express my gratitude to my family, especially, my parents for their moral support and warm encouragements.